On the bimodal dynamics of the turbulent horseshoe vortex system in a wing-body junction

Joongcheol Paik, Cristian Escauriaza,[a] and Fotis Sotiropoulos[b]
St. Anthony Falls Laboratory, University of Minnesota, Minneapolis, Minnesota 55414

The turbulent boundary layer approaching a wall-mounted obstacle experiences a strong adverse pressure gradient and undergoes three-dimensional separation leading to the formation of a dynamically rich horseshoe vortex (HSV) system. In a pioneering experimental study, Devenport and Simpson [J. Fluid Mech. **210**, 23 (1990)] showed that the HSV system forming at the leading edge region of a wing mounted on a flat plate at $Re = 1.15 \times 10^5$ exhibits bimodal, low-frequency oscillations, which away from the wall produce turbulent energy and stresses one order of magnitude higher than those produced by the conventional shear mechanism in the approaching turbulent boundary layer. We carry out numerical simulations for the experimental configuration of Devenport and Simpson using the detached-eddy-simulation (DES) approach. The DES length scale is adjusted for this flow to alleviate the well known shortcoming of DES; namely that of premature, laminar-like flow separation. The numerical simulations reproduce with good accuracy most experimental observations, including both the distributions of the mean flow and turbulence quantities and the bimodal dynamics of the velocity field in the HSV region. The only remaining discrepancy between experiments and simulations is the predicted location of the HSV, which is somewhat further upstream from the wing than the measured one. Proper orthogonal decomposition (POD) of the resolved flow field is employed to gain insights into the coherent dynamics of the flow. The POD analysis shows that 85% of the energy in the vortex region is accounted for by the first two POD modes whose dynamics is quasiperiodic. To elucidate the physical mechanisms that lead to the onset of the bimodal dynamics, we employ probability-density-function-based conditional averaging and visualization of the instantaneous three-dimensional structure of the HSV using the q criterion. We show that the bimodal dynamics is due to the continuous and aperiodic interplay of two basic states: an organized state with a coherent necklace-like HSV, and a disorganized state with hairpin vortices wrapping around the HSV. We argue that the emergence of hairpin vortices is the result of centrifugal instability. © *2007 American Institute of Physics*. [DOI: 10.1063/1.2716813]

I. INTRODUCTION

The turbulent boundary layer approaching a wall-mounted obstacle experiences a strong adverse pressure gradient and undergoes three-dimensional separation forming a horseshoe vortex (HSV) that wraps around the obstacle-like necklace. HSV flows past wall mounted obstacles are encountered in many applications of practical interest in hydrodynamics, hydraulics, and aerodynamics and for that reason they have attracted considerable attention both experimentally and computationally. Various generic junction configurations have been studied so far, including wall mounted wings,[1] cubes,[2,3] and circular cylinders.[4–6] A recent comprehensive review of past experimental studies of such flows and extensive discussion of their underlying physics can be found in Simpson.[7]

The most striking finding of previous experiments is that the turbulent HSV is dominated by coherent, low-frequency unsteadiness and characterized by bimodal histograms of velocity probability density functions (pdfs).[1–3,6] This impor-

tant feature of the flow was first demonstrated experimentally and discussed in detail in the pioneering work of Devenport and Simpson,[1] who carried out experiments for the flow past a wall-mounted wing at $Re = 1.15 \times 10^5$, based on the bulk velocity and the maximum thickness of the wing. They reported[1] that the HSV undergoes bimodal, low-frequency oscillations between two basic states: the so-called *backflow* mode, when the return HSV flow—i.e., the flow that is directed from the wing leading edge toward the upstream direction along the flat plate—is able to penetrate far upstream forming a strong wall jet; and the *zero-flow* mode, when the return flow is unable to penetrate upstream and is ejected vertically upward away from the wall. Devenport and Simpson[1] further showed that the bimodal, coherent oscillations of the HSV region produce turbulent stresses one order of magnitude larger than those produced by the classical shear mechanism inside the approaching turbulent boundary layer.

The experimental configuration of Devenport and Simpson[1] has been extensively studied numerically using steady Reynolds-averaged Navier-Stokes (RANS) turbulence models, including linear and nonlinear eddy viscosity models and second-moment closure models.[8–11] The main conclu-

sions from these studies can be summarized as follows. RANS simulations employing linear and nonlinear eddy viscosity models in general fail to capture the location and the shape of the mean HSV as well as the increased turbulence statistics in the vicinity of the junction.[8,9,11] Second-moment closure models have been shown to perform much better than eddy-viscosity models. Such models can capture both the size and the core location of the mean HSV and also reproduce, at least to some degree, the increased turbulence intensities in the junction region provided that the near-wall region is resolved carefully.[8,10,11] Even these more refined RANS models, however, have not been able to capture certain distinct features of the measurements of Devenport and Simpson such as, for example, the C-shaped, double-peak distribution of the turbulence kinetic energy. Naturally such models are inherently limited by the statistically steady flow they can simulate, and as such they should not be expected to yield any insights into the bimodal dynamics of the flow. The limitations of standard RANS methods for this flow were also identified and pointed out in the original paper of Devenport and Simpson[1] and also discussed in the recent review by Simpson.[7]

Large-eddy simulation (LES) can in principle resolve the rich dynamics of HSV flows, and several such studies have been reported in the literature.[12–15] Due to the high Reynolds number of Devenport and Simpson flow, however, LES studies have focused on the flow past a wall mounted cube for which experiments are available at Re=40000,[2,3] based on the inlet bulk velocity and the height of the cube. Steady and unsteady RANS simulations have also been reported for this test case with essentially the same general conclusions as those discussed above for the Devenport and Simpson flow.[12,16,17] It is important to point out that unsteady RANS (URANS) models have failed to capture the unsteadiness in the HSV region even when second-moment closure models are employed.[17] All LES studies have reported that the calculated flow in the HSV region exhibits bimodal oscillations, thus confirming the experimental findings.[12–15] These studies, however, have focused primarily on the prediction of separation from the sharp edges of the cube and have not provided any further details about the nature of the HSV oscillations beyond mentioning that the velocity pdfs in the HSV region are indeed bimodal.[13–15] An important finding from the LES computations is that the specification of time-dependent, turbulent-like inflow boundary conditions is a critical prerequisite for accurately predicting the experimentally observed location of the HSV. LES with steady inflow conditions appear to capture the unsteadiness in the junction region, but the calculated HSV is somewhat upstream from its measured location.[13,15] In a more recent study, Yakhot et al.[18] carried out direct numerical simulation (DNS) for turbulent flow past a wall mounted cube at Re=5610, based on the bulk velocity and the channel height. Interestingly, this simulation was able to capture the overall features of the measured[2] flow (HSV size and the location) in spite of the order of magnitude difference in the Reynolds number.

It is evident from the above literature review that even though progress has been made in the prediction of HSV flows, several important aspects of the problem remain either poorly understood or entirely unexplored. For instance, even though LES studies have yielded bimodal HSV flow fields, neither the exact nature of the bimodal oscillations (i.e., the physics of the backflow and zero-flow modes[1]) nor the underlying mechanisms that lead to their onset are fully understood. Moreover, the unsteady coherent dynamics of the HSV at the range of Reynolds numbers considered by Devenport and Simpson[1] have yet to be reproduced computationally. Our work is motivated by and seeks to contribute to addressing these gaps in our fundamental understanding of turbulent HSV flows.

We carry out unsteady numerical simulations for the Devenport and Simpson[1] experiment using a coherent-structure resolving turbulence model. Since fully resolved LES at the range of Reynolds numbers studied by Devenport and Simpson[1] (Re=1.15×10^5) is not within the reach of computational resources at our disposal, we employ the detached eddy simulation (DES) approach developed by Spalart et al.[19] The standard DES and similar hybrid URANS/LES approaches are known to suffer from grid-induced, nonphysical separation in regions where the mesh spacing violates the conditions based on which the original approach was developed—namely, that the grid spacing in the direction parallel to the wall must be much greater than at least half the thickness of the boundary layer.[19–21] In the case under consideration, this condition is inevitably violated in the junction region between the wing and the wall, where the grid in both the streamwise and vertical directions needs to be refined to accurately resolve the HSV. To remedy this modeling shortcoming, we adjust herein the DES length scale to ensure that a URANS layer is always present near the wall regardless of the local grid spacing. The distance from the wall where the URANS-to-LES transition occurs is placed halfway between the location of the mean HSV core and the wall. The governing equations are solved using a second-order accurate, dual-time-stepping artificial compressibility method. A chimera overset grid layout is used to efficiently discretize the wall-mounted wing configuration and to embed fine mesh resolution in the immediate vicinity of the wing leading edge where the HSV forms. The grid sensitivity of the computed solutions is examined by carrying out simulations on two meshes refined by a factor of 3/2 in all three directions. The fine mesh consists of 6.2 million grid nodes with approximately half of these nodes embedded within the HSV region. The computed solutions are compared with the experimental measurements of Devenport and Simpson[1] in terms of mean pressure and vorticity contours, limiting streamlines on the flat wall, and turbulence statistics at the HSV plane of the symmetry. It is shown that our simulations capture most experimental features with good accuracy. We analyze our computed solutions using the proper orthogonal decomposition (POD),[22] a new pdf-based conditional averaging approach, and visualization of the three-dimensional coherent structures to elucidate the rich dynamics of the HSV and to clarify the three-dimensional structure of the two modes.

The paper is organized as follows. First, we present the governing equations and a brief description of the numerical approach and various computational details. Next we discuss

the features of the time-averaged flow and turbulent statistics and compare our computations with the experimental measurements.[1] This is followed by the POD analysis of the resolved flow fields. Subsequently, conditional averaging and visualization of the instantaneous coherent structures are used to elucidate the physics of the flow. Finally, we summarize our findings and discuss future research needs.

II. NUMERICAL METHODOLOGY

A. Governing equations

The governing equations for the mean flow are the three-dimensional, unsteady, incompressible, Reynolds-averaged Navier-Stokes (RANS) equations. The equations are formulated in generalized curvilinear coordinates and read in strong-conservation form as follows:

$$\Gamma \frac{\partial Q}{\partial t} + J \frac{\partial}{\partial \xi^j}(F^j - F_v^j) = 0, \tag{1}$$

where

$$\Gamma = \mathrm{diag}[0,1,1,1],$$

$$Q = [P, u_1, u_2, u_3]^T,$$

$$F^j = \frac{1}{J}[U^j, u_1 U^j + P\xi_{x_1}^j, u_2 U^j + P\xi_{x_2}^j, u_3 U^j + P\xi_{x_3}^j]^T,$$

$$F_v^j = \frac{1}{J}\left(\frac{1}{\mathrm{Re}} + \nu_t\right)\left[0, g^{mj}\frac{\partial u_1}{\partial \xi^m} + R_{m1}\xi_{x_m}^j, g^{mj}\frac{\partial u_2}{\partial \xi^m}\right.$$
$$\left. + R_{m2}\xi_{x_m}^j, g^{mj}\frac{\partial u_3}{\partial \xi^m} + R_{m3}\xi_{x_m}^j\right]^T.$$

In the equations above, the term P is a modified pressure $P = p/\rho + 2k/3$, where p is the piezometric pressure and k is the turbulence kinetic energy, u_i ($i=1,2,3$) are the resolved Cartesian velocity components, x_i are the Cartesian coordinates, J is the Jacobian of the geometric transformation, $\xi_{x_i}^j$ are the metrics of the geometric transformation, U^j are the contravariant velocity components $U^j = u_i \xi_{x_i}^j$, g^{ij} are the components of the contravariant metric tensor $g^{ij} = \xi_{x_k}^i \xi_{x_k}^j$, Re is the Reynolds number, ν_t is the turbulent viscosity, which is introduced by adopting Boussinesq's assumption for modeling the unresolved stresses, and R_{ij} is the velocity gradient tensor $R_{ij} = (\partial u_j / \partial \xi^k)\xi_{x_j}^i$.

B. DES model

Detached-eddy simulation (DES) was proposed by Spalart et al.[19] and is based on the Spalart-Allmaras (SA) one-equation eddy viscosity model,[23] which solves a single transport equation for a working variable $\tilde{\nu}$ that is related to the turbulent viscosity ν_t. This model includes a wall destruction term, which reduces the turbulent viscosity in the logarithmic layer and laminar sublayer, as well as transition terms, which provide a smooth transition from laminar to turbulent flow.[23] After neglecting the transition terms, which are not necessary in the present simulations, the transport equation reads as follows:

$$\frac{1}{J}\frac{\partial \tilde{\nu}}{\partial t} + \frac{\partial}{\partial \xi^j}[F_t^j - F_{tv}^j] + H_t = 0, \tag{2}$$

where

$$F_t^j = \frac{1}{J}[U^j \tilde{\nu}],$$

$$F_{tv}^j = \frac{1}{J}\left[\frac{1}{\sigma}\left(\frac{1}{\mathrm{Re}} + \tilde{\nu}\right)g^{mj}\frac{\partial \tilde{\nu}}{\partial \xi^m}\right],$$

$$H_t = \frac{1}{J}\left[-c_{b1}(1-f_{t2})\tilde{S}\tilde{\nu} + \left(c_{w1}f_w - \frac{c_{b1}}{\kappa^2}f_{t2}\right)\left(\frac{\tilde{\nu}}{d}\right)^2\right.$$
$$\left. - \frac{1}{\sigma}c_{b2}g^{mj}\frac{\partial \tilde{\nu}}{\partial \xi^m}\frac{\partial \tilde{\nu}}{\partial \xi^m}\right].$$

The turbulent viscosity ν_t is linked to the working variable $\tilde{\nu}$ and a wall function $f_{\nu1}$ by

$$\nu_t = \tilde{\nu}f_{\nu1}, \quad f_{\nu1} = \frac{\chi^3}{\chi^3 + c_{\nu1}^3}, \quad \chi = \frac{\tilde{\nu}}{\nu}, \tag{3}$$

where ν is the molecular viscosity. The modified vorticity $\tilde{S}$ is defined in terms of the magnitude of the vorticity S as

$$\tilde{S} \equiv f_{\nu3}S + \frac{\tilde{\nu}}{\kappa^2 \tilde{d}^2}f_{\nu2}, \quad f_{\nu2} = \left(1 + \frac{\chi}{c_{\nu2}}\right)^{-3}, \tag{4}$$

$$f_{\nu3} = \frac{(1+\chi f_{\nu1})(1-f_{\nu2})}{\chi},$$

where $\tilde{d}$ is the DES length scale (see below). The production term as written in Eq. (4) differs from that developed by Spalart and Allmaras[23] via the introduction of $f_{\nu3}$ and redefinition of $f_{\nu2}$. These changes do not alter predictions of fully turbulent flows and have the advantage that in simulation of flows with laminar separation, spurious upstream propagation of the eddy viscosity into attached, laminar regions is prevented.[24] The wall destruction function f_w is given as follows:

$$f_w = g\left[\frac{1+c_{w3}^6}{g^6 + c_{w3}^6}\right]^{1/6}, \quad g = r + c_{w2}(r^6 - r), \quad r \equiv \frac{\tilde{\nu}}{\tilde{S}\kappa^2 \tilde{d}^2}, \tag{5}$$

where

$$f_{t2} = c_{t3}\exp(-c_{t4}\chi^2). \tag{6}$$

The closure coefficients are

$$c_{b1} = 0.1355, \quad \sigma = 2/3, \quad c_{b2} = 0.622,$$

$$\kappa = 0.41, \quad c_{w1} = c_{b1}/\kappa^2 + (1+c_{b2})/\sigma, \quad c_{w2} = 0.3,$$

$$c_{w3} = 2, \quad c_{\nu1} = 7.1, \quad c_{t3} = 1.1, \quad c_{t4} = 2. \tag{7}$$

The DES length scale in the above equations depends on the distance from the nearest wall d and the local grid spacing Δ as follows:

$$\widetilde{d} \equiv \min(d, C_{DES}\Delta), \tag{8}$$

where $\Delta \equiv \max(\Delta x, \Delta y, \Delta z)$ is the largest dimension of the grid cell and the additional model constant is set equal to its standard value, $C_{DES} = 0.65$, which was obtained after calibration of the model for homogeneous turbulence.[25] Assuming that the computational mesh is constructed such that the wall-parallel grid spacing is of the order of the boundary layer thickness, the above length scale definition ensures that the SA URANS model is retained throughout the boundary layer, i.e., $\widetilde{d} = d$. Consequently, prediction of boundary layer separation is determined in the URANS mode of DES. Sufficiently far from solid boundaries $\widetilde{d} \sim \Delta$, and the model becomes a one-equation LES model for the subgrid scale (SGS) eddy viscosity. When the production and destruction terms of the model are balanced, the length scale $\widetilde{d} = C_{DES}\Delta$ in the LES region yields a Smagorinsky eddy viscosity $\widetilde{\nu} \propto S\Delta^2$. Analogous to classical LES, the role of Δ is to allow the energy cascade down to the grid size; roughly, it makes the pseudo-Kolmogorov length scale, based on the eddy viscosity, proportional to the grid spacing.

As already discussed, with the above standard DES model, the boundary layers are treated entirely with URANS mode by generating an RANS grid with large grid spacing parallel to the wall, which is common practice in conventional wall-resolving RANS calculations. In the present case, however, the HSV resides inside the boundary layer at the junction between two walls (the flat plate and the wing surface) and the computational grid needs to be refined both in the streamwise (direction normal to the wing surface) and vertical (direction normal to the flat plate) directions to accurately resolve the vortex structure (see Fig. 2). Consequently, the resulting grid spacing in both spatial directions (streamwise and vertical) in the junction region has to be significantly smaller than the boundary layer thickness. From the DES standpoint, such grid structure implies that the LES mode of the model will be activated prematurely in the attached region of the flow where coherent unsteadiness has not yet emerged in the computed solutions. Consequently, the instantaneous flow fields do not have a sufficient level of Reynolds stresses to support a turbulent-like LES computation, and the flow separates in a laminar fashion. This strong dependence of the DES and similar hybrid URANS/LES approaches on the grid structure has been recognized by Spalart[19] and also discussed and demonstrated by others in recent studies.[21,20] Our first attempt to apply the standard DES model to the HSV problem verified these findings as the computed flow fields in the HSV vortex region were overenergized and laminar-like (see the next section).

C. Adjusted DES model

In order to mitigate the grid-induced premature separation of the standard model, we propose a simple adjustment of the original DES length scale given by Eq. (8), which is guided by the experimentally known physics of the flow under consideration. The proposed definition seeks to enforce the presence of a URANS layer regardless of the local grid spacing in order to prevent the interface of URANS and LES

regions from being situated too close to the wall. To accomplish this, we introduce a new length scale d_ℓ based on the height of the measured mean HSV core from the wall H_{core}. More specifically, the proposed length scales reads as follows:

$$\widetilde{d}_n = \begin{cases} d & \text{if } d \leq d_\ell \\ \min(d, C_{DES}\Delta) & \text{if } C_{DES}\Delta \geq d_\ell \\ (1-f_\ell)C_{DES}\Delta + f_\ell d_\ell & \text{otherwise} \end{cases} \tag{9}$$

where

$$d_\ell \simeq \frac{H_{core}}{2},$$

$$f_\ell = \exp\left[-\left(\frac{d - d_\ell}{d_\ell - C_{DES}\Delta}\right)^3\right].$$

The vertical profiles of the proposed composite length scale $\widetilde{d}_n$ of Eq. (9) and the standard DES length scale $\widetilde{d}$ of Eq. (8) at a streamwise location within the HSV region are shown in Fig. 3. When the interface of URANS and LES regions according to the standard definition is located inside the attached region, the adjusted length scale acts to push the URANS-LES interface upward in the outer region of the boundary layer. The exponential function used in the Eq. (9) further ensures that the transition from the URANS to the LES modes of the model takes place in a smooth manner. It is important to note that the length scales calculated by both definitions are identical in the region above the mean HSV core.

The specific functions used in Eq. (9) along with the $H_{core}/2$ location where the transition from the URANS to the LES starts were selected after extensive numerical experiments in order to obtain the best overall agreement with the experimental measurements in the HSV region. These numerical tests showed that when d_ℓ is placed too close to the wall, premature laminar-like separation is not prevented. At the other extreme, if d_ℓ is placed at a distance from the wall such that the entire HSV vortex is contained within the URANS region of the model, the solution eventually converges to the steady RANS solution with no large-scale dynamics. As the subsequently presented comparisons between our simulations and the experimental measurements of Devenport and Simpson[1] will show, placing the URANS/LES interface halfway between the mean HSV vortex core and the wall not only eliminates the spurious, laminar-like separation, but also captures the onset of bimodal dynamics, resolves directly essentially all energy-producing scales of motion in the HSV region, and yields overall turbulence levels that are in good qualitative and quantitative agreement with the measurements.

It is important to point out that with the adjusted length scale given by Eq. (9), the unsteadiness is not excited only in the LES region of the model but originates deep into the URANS layer of the model (i.e., the lower half of the region between the mean HSV core and the wall) presumably due to the unsteady forcing imposed by the former (LES region) on the latter. In fact, we will subsequently show that the bimodal dynamics of the flow, which according to the experiment
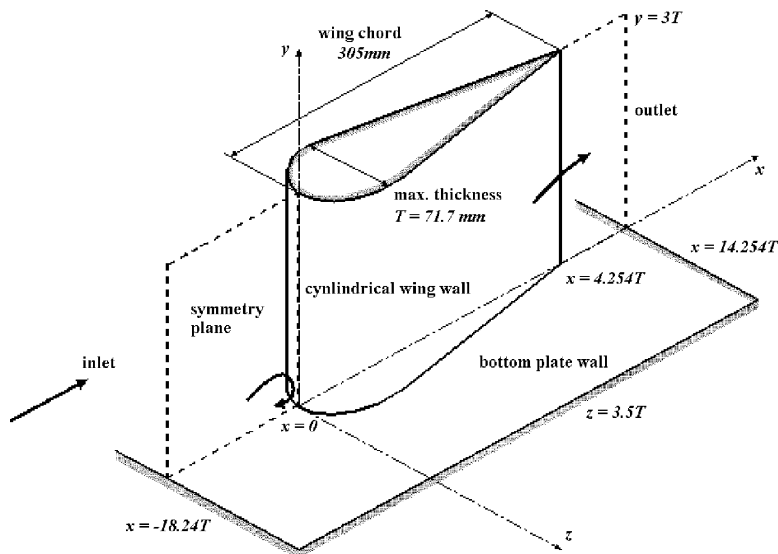
FIG. 1. Schematic view of the wing-body junction flow and the geometrical configuration of the computational domain according to the ERCOFTAC guidelines of Devenport and Simpson[1] (see Case 08 Wing-body junction with separation at http://cfd.me.umist.ac.uk/ercorftac/).

occurs entirely within the URANS layer of the adjusted model (see Fig. 11 below), is driven by the onset of very rich and highly energetic unsteady coherent structures. These structures are resolved by the adjusted length-scale definition in the URANS mode of the model.

D. The numerical method

The governing equations are solved using a dual-time-stepping artificial compressibility (AC) iteration scheme. The AC form of the governing equations is discretized using a second-order-accurate finite-volume method on a nonstaggered computational grid. The convective terms are discretized using the second-order accurate, upwind biased QUICK scheme, and central differencing is employed for the pressure gradients, viscous fluxes, and source terms in the turbulence equation. The third-order, fourth-difference artificial dissipation method of Sotiropoulos and Abdallah[26] is employed for pressure to eliminate odd-even decoupling of the pressure field. The physical time derivatives are discretized with a three-point-backward, Euler-implicit temporal-integration scheme. The discrete equations are marched in time to advance the solution to the next time step by adopting the dual- (or pseudo-) time-stepping method. The system of equations is integrated in pseudo time using the pressure-based implicit preconditioner[27] enhanced with local-time-stepping and V-cycle multigrid acceleration. The complex wing geometry is handled using the domain-decomposition approach with structured, overset (chimera) grids. We apply a set of characteristics-based, nonreflecting boundary conditions at the outlet of the computational domain to allow complex vortical structures to exit the computational domain without distortion. The numerical method has been extensively evaluated for calculating various turbulent shear flows in complex geometrical configurations.[27–29] For a detailed description of the numerical method, the reader is referred to Paik et al.[27]

E. Computational details

We simulate flow past the wall-mounted cylindrical wing configuration studied experimentally by Devenport and Simpson.[1] The geometry of the computational domain and the coordinate system for the junction flow are depicted in Fig. 1. The cylindrical wing has a maximum thickness of $T = 71.7$ mm and a chord length of 305 mm. It is located $18.24T$ downstream from the inlet and has its cord aligned with the x-axis. The wing cross section consists of a $3:2$ elliptical nose (major axis aligned with the chord) and a NACA 0020 tail joined at the maximum thickness. The experiments of Devenport and Simpson[1] were carried out at Reynolds number $Re = 1.15 \times 10^5$, based on the maximum thickness T and the approaching bulk velocity U_0.

The locations of the various boundaries of the computational domain are selected according to the ERCOFTAC guidelines (see Case 08 Wing-body junction with separation at http://cfd.me.umist.ac.uk/ercorftac/ for details). The inflow boundary is placed at $x/T = -18.24$, where the boundary layer is prescribed using the experimental measurements[1] at the same station. The so-prescribed inlet flow corresponds to a tripped, two-dimensional boundary layer developing under
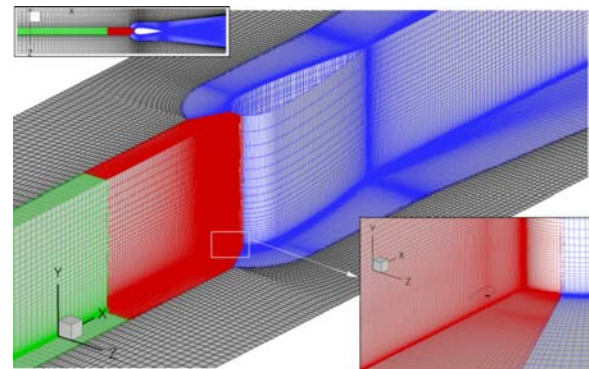

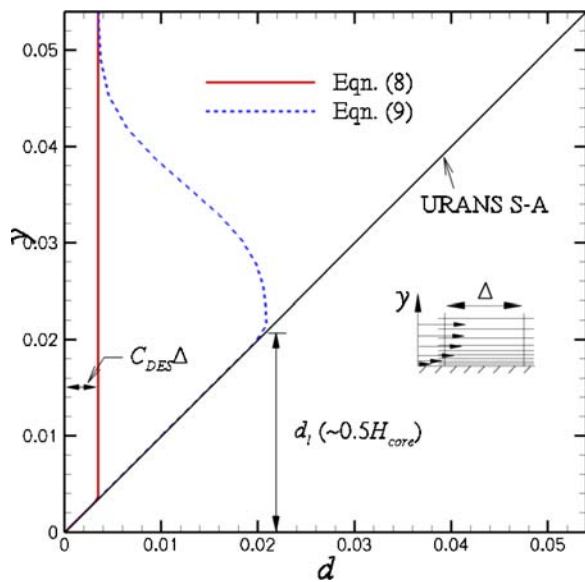FIG. 2. Computational overset grid system.

FIG. 3. DES length scales computed using Eqs. (8) and (9) along a vertical line upstream of the wing.

zero pressure gradient conditions. The eddy viscosity and the turbulence working variable $\tilde{\nu}$ required by the DES model at the inlet are precalculated using the mixing-length prescription of Norris and Reynolds[30] and the turbulence kinetic energy measured by Devenport and Simpson.[1] The outlet boundary is placed at $x=14.254T$, where the aforementioned nonreflecting characteristic boundary conditions are applied. The lateral boundaries are placed symmetrically with respect to the wing vertical plane of symmetry at $z=\pm3.5T$ while the boundary parallel to the bottom wall is placed at $y=3T$. Zero gradient boundary conditions are used at all these boundaries. No-slip boundary conditions are applied on the bottom wall and the wing surface.

The computational domain is discretized using domain decomposition with overset grids. A Cartesian grid is used for the background computational domain in the region away from the wing. A curvilinear, body-fitted, C-type grid is embedded within the background grid to discretize the region around the wing as shown in Fig. 2. Additional C-type subdomains are further embedded in the leading-edge region of the wing to ensure fine numerical resolution in the vicinity of the HSV system. Note that embedding C-type grids around the surface and near the leading edge of the wing allow for the efficient clustering of grid nodes in the region of interest without unnecessarily burdening the rest of the computational domain with the high aspect ratio cells that would result if the entire computational domain were to be discretized with a single set of coordinates.

To examine the grid sensitivity of the computed solutions, we carry out numerical simulations on two computational meshes. The *coarse* overset grid layout consists of a total of 1.9×10^{6} grid nodes with approximately 1.0×10^{6} of these nodes embedded in the leading-edge region of the wing at the junction with the flat plate. The *fine* grid system is constructed by increasing the number of grid nodes by factor of $3/2$ along each of the three curvilinear directions. The total number of active grid nodes in the *fine* grid layout is

6.2×10^{6}, of which 3.5×10^{6} grid nodes are clustered in the leading-edge junction region. The first grid node off of all solid walls has been left unchanged on both grids and is located at $y^{+}\leq0.5$ everywhere on both meshes. The *coarse* and *fine* grid simulations are carried out using nondimensional physical time steps of $\Delta t=0.01$ and 0.007, respectively.

Calculations were carried out with the original and adjusted DES models on both the *coarse* and *fine* meshes. As we will subsequently show, the solution obtained with the standard DES model is dominated by spurious, laminar-like separation in the HSV region (see Sec. III A below). Thus, the mesh refinement study for the standard model was carried out in order to examine whether a finer mesh could eliminate or somehow alter this nonphysical phenomenon, but the results were identical on both meshes. For the adjusted DES model, the *fine* mesh solution yielded somewhat better agreement with the measurements than the *coarse* mesh solution, but in general the calculated flow fields on both grids were very similar to each other. The location of the upstream separation point and the structure of the HSV were not affected significantly by the grid density. In addition, all the subsequently discussed dynamics of the flow were reproduced with similar accuracy on both meshes. The only notable difference between the two numerical solutions was the small overestimation of the resolved stresses and turbulence kinetic energy on the *coarse* mesh relative to the *fine* mesh solution. In conclusion, our grid sensitivity study showed that when the adjusted DES model is used, even the coarse mesh is adequate for capturing all essential dynamics of the flow with the fine mesh improving somewhat the agreement with the measurements. All subsequently presented results were obtained on the *fine* mesh.

III. RESULTS AND DISCUSSION

We begin the presentation and discussion of the computed results by focusing on the time-averaged features of the flow. We first discuss the effect of the DES length scale on the calculated flow and compare our simulations with the experimental measurements.[1] We then shift our focus to the rich dynamics of the resolved flow fields. We establish the bimodal nature of the HSV and explore its dynamics using the proper orthogonal decomposition.[22] Finally, we elucidate the physical mechanisms that give rise to the bimodal oscillations using conditional averaging and 3D visualization of the coherent structures in the HSV region.

A. Mean flow and turbulence statistics comparisons

The measured[1] out-of-plane component of the time-averaged vorticity field and the mean flow streamlines at the plane of symmetry in the junction region are shown in Fig. 4(a). The measurements reveal a number of distinct features of the time-averaged HSV. The wing-plate junction region is occupied by an approximately elliptical in shape HSV whose sense of rotation is in the clockwise direction (negative vorticity). The HSV core has a distinct thin but long tail of negative vorticity that emanates from the vortex core and stretches upstream parallel to the flat plate. The presence of
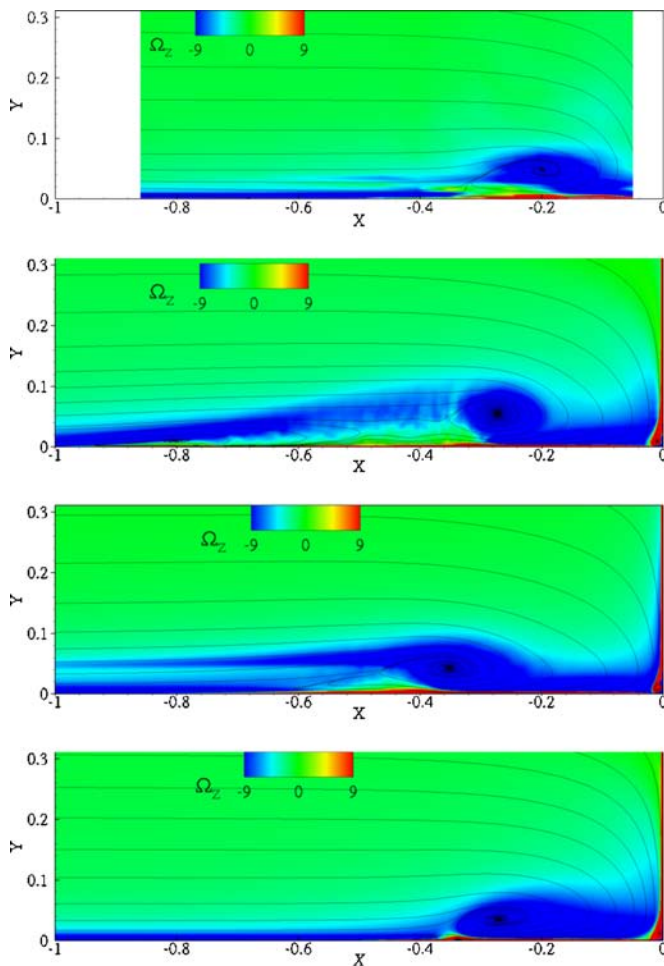
FIG. 4. Time-averaged vorticity distribution and streamlines at the plane of symmetry upstream of the wing: (a) the measurement,[1] (b) the standard DES solution, (c) the adjusted DES solution, and (d) the RANS solution.

this vorticity tail is consistent with the measured mean streamwise velocity profiles in the vertical direction upstream of the HSV core. As seen in Fig. 5 in Devenport and Simpson,[1] the mean velocity profiles upstream of the HSV core exhibit a clearly visible kink across the region occupied by the aforementioned tail of vorticity. Devenport and Simpson[1] did not discuss the possible cause for this feature of their measurements, which, as we will subsequently show, is also captured by the present simulations. Another thin layer of negative vorticity is also observed in the measurements along the flat plate below the HSV vorticity tail. This lower, wall-attached vorticity layer, which starts from upstream, slightly lifts off the wall from the saddle point of separation at $X/T=-0.48$ and terminates just upstream of the mean HSV approximately at $X/T=-0.35$.

An important feature of the measured vorticity field that follows from Fig. 4(a) is the existence of a thin positive layer of vorticity just below the HSV core. This layer appears to emanate near the junction corner and stretches to the saddle of separation along the wall below the HSV. The overall magnitude of positive vorticity is similar to that of the negative vorticity upstream of the saddle of separation. The presence of this positive vorticity layer suggests a strong interaction of the HSV with the flat plate, which leads to the

extraction of wall vorticity of opposite sign. It is worth emphasizing here that the instantaneous flow fields in the upper half of this positive vorticity layer are characterized by bimodal histograms of velocity fluctuations with two peaks of a similar magnitude of streamwise velocity pdfs (see Sec. III B for details).

In addition to the experimental measurements, Fig. 4 also includes the time-averaged results obtained with the standard and adjusted DES models and the RANS model using the SA model,[23] Figs. 4(b)–4(d), respectively. Note that the solution shown in Fig. 4(d) is obtained regardless of whether the SA model is run in a steady or unsteady RANS mode. The results from the standard DES model are included in order to illustrate its poor performance in the HSV region. Even though it is not shown herein, the instantaneous flow fields obtained with the standard DES model show that the flow separates in a spurious laminar-like manner. The so-computed HSV vortex is overenergized and the resulting resolved turbulence kinetic energy grossly overestimates the measured kinetic energy (see below for comparisons of measured and computed turbulence kinetic energy fields). The time-averaged vorticity field and streamlines shown in Fig. 4(b) clearly show the effect of the overenergetic, laminar-like separation on the mean flow. The calculated flow field does not exhibit any of the experimental trends. The upstream separation point is located at $X/T=-0.95$ and the calculated primary HSV core is more rounded rather than elliptic. The calculated streamlines reveal the presence of two saddle foci at the symmetry plane (as compared to a single vortex core in the experiment) suggesting a multivortex structure, which is very much reminiscent of a laminar HSV.[31] Furthermore, the previously discussed double-layer structure upstream of the vortex core is not captured by the standard DES model. In fact, the calculated vorticity field exhibits a single-layer structure upstream of the HSV ($-1 \leq x/T \leq -0.6$), which is thicker and of significantly higher magnitude than the measured vorticity field in the same region and lifts off the wall in a nonphysical manner. It is interesting that, in spite of the premature separation, the location of the time-averaged HSV core computed by the standard DES coincides with the RANS solution yielding the HSV core approximately at $X/T=-0.28$, as shown in Fig. 4(d). The RANS solution also confirms the previous discussion by Pasinato et al.[32] that the SA turbulence closure model is sensitive to the adverse pressure gradient. In summary, the standard DES model yields a HSV structure that does not resemble the measurements either qualitatively or quantitatively.

The implementation of the adjusted DES length scale has a profound effect on the calculated mean HSV structure, as shown in Fig. 4(c). The computed vortex core is now clearly elliptical and more slender in agreement with the measurements, and the overall magnitude of the calculated vorticity field is in good agreement with the experiment. Furthermore, the double-layer structure of the measured vorticity field upstream of the HSV is now captured by the simulation even though the calculated upper negative vorticity layer (the HSV vorticity tail) appears somewhat stronger in magnitude than the measured layer. This discrepancy, however, could be reasonably attributed to the inherent difficul-

ties in resolving such a thin layer of vorticity experimentally. The calculated vorticity field also captures the positive layer of vorticity below the HSV core. Both the thickness and the levels of the positive vorticity within this layer are in good agreement with the measurements. The only notable discrepancy between experiments and simulations is in the location of the HSV core, which is now located roughly at $X/T=$ -0.36 as compared to $X/T=-0.20$ in the measurements. The standard DES and SA models yield a vortex core at $X/T=$ -0.28, which is closer to the measured location. The vertical distance of the HSV core from the wall predicted by the adjusted DES model is in between the standard DES and SA predictions. The corresponding locations in the experiment, and the adjusted DES, standard DES, and SA predictions, are $Y/T=0.048$, 0.044, 0.055, and 0.035, respectively.

It is important to emphasize that even though the vorticity field computed by the adjusted DES does suggest that the simulated flow separates somewhat earlier than in the experiment, the resulting flow field is fundamentally different from that obtained with the standard DES. As discussed above, in the latter case the separation occurs further upstream and is essentially laminar in nature. In the case of the adjusted model, however, we will subsequently show that the calculated flow exhibits essentially all experimental trends both instantaneously and on average and that the only remaining discrepancy with the measurements is the precise location of the mean HSV. All subsequently presented results have been obtained with the adjusted DES model.

Devenport and Simpson[1] reported oil-flow visualization of the limiting streamlines (or friction lines) on the flat wall, which is shown in Fig. 5(a). The experimental image reveals the presence of two distinct lines wrapping around the wing. The line farther away from the wing is a line of separation, which originates at the saddle point at the plane of symmetry [see Fig. 4(a)] and marks the location where the approach boundary layer undergoes three-dimensional separation due to the adverse pressure gradient imposed by the wing. The second line is located closer to the wing and, as pointed out by Devenport and Simpson,[1] is a line of low streamwise shear. This line marks the boundary between the low shear stress region away from the wing and the high shear region in its immediate vicinity.[1] In Fig. 5(b), we plot the calculated mean friction lines on the bottom wall colored with the mean friction velocity u_τ. It is seen that the computed solution captures the presence of the two lines and further confirms that the inner line in indeed a line of low shear that delineates the regions of low (outer) and high (inner) shear stress. As also observed in the experimentally visualized friction lines, the two lines merge together at a distance approximately equal to $1.4T$ from the leading edge. To further clarify the nature of the second line in the limiting streamlines plot, we show in Fig. 5(c) root-mean-square (RMS) contours of the resolved friction velocity field. It is evident from this figure that the near wall flow is essentially stationary around the separation line while a C-shaped pocket of nonzero fluctuations of the near wall velocities exists in the interior of the line of low shear. In fact, the line of low shear is seen to perfectly demarcate the outer boundary of the region of increased RMS of the shear velocity that wraps around the
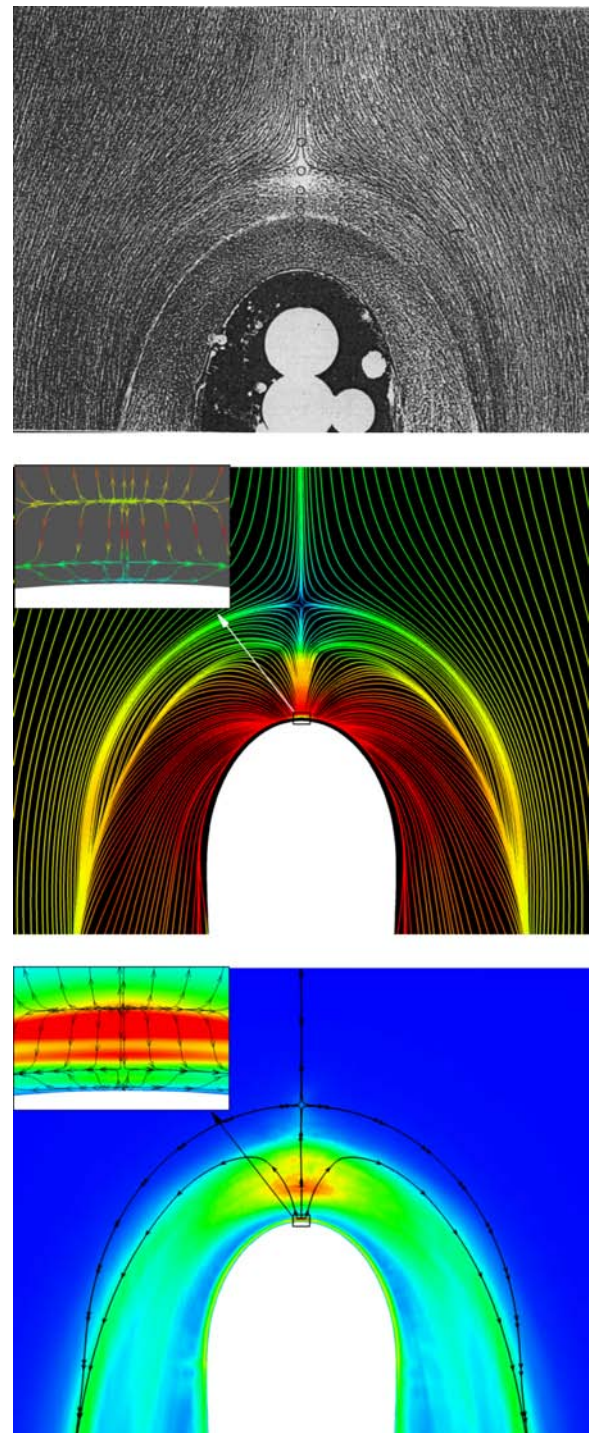

FIG. 5. Visualization of limiting streamlines on the bottom surface: (a) surface oil-flow visualization performed by Devenport and Simpson[1]; (b) time-averaged limiting streamlines colored by time-averaged shear velocity (blue, $u_\tau=0$ and red, $u_\tau=0.07$); and (c) contours of RMS of fluctuating shear velocity [blue, RMS$(u'_\tau)=0$ and red, RMS$(u'_\tau)=0.02$]. Each inset in (b) and (c) shows a magnification of the flow near the nose of the wing to clarify the complex topology in this region.

wing. Devenport and Simpson[1] also comment that although not clearly visible in their oil-flow visualizations, a small region of secondary separation also exists in the corner between the wall and the wing. This feature of the flow is also captured by our simulations, as shown in the insets in Fig. 5, where we have magnified the topology of the flow in the immediate vicinity of the wing leading edge.
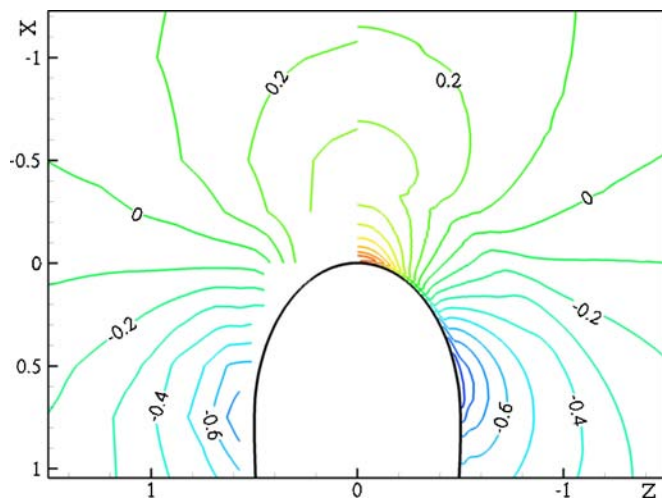
FIG. 6. Comparison of the measured[1] (left half) and the computed (right half) mean pressure coefficient C_p in the vicinity of the wing nose.

FIG. 7. Contours of (a) the resolved turbulence kinetic energy and (b) the measured[1] turbulence kinetic energy at the plane of symmetry.

Figure 6 compares measured[1] and computed contours of the time-averaged pressure coefficient C_p on the bottom wall in the vicinity of the wing leading edge. It is seen that the calculated pressure field is in good overall agreement with the measurements. It is worth noting in this figure that the calculated pressure contours exhibit a distinct kink along a line that corresponds to the secondary line of separation in Fig. 5. Such a kink is not present in the experimental measurements shown in Fig. 6. We should point out, however, that the data plotted in this figure were downloaded from the ERCOFTAC website. The actual figure included in the original paper of Devenport and Simpson,[1] however, does show a very similar kink in the measured pressure contours to that observed in our simulations (see the upper half of Fig. 3 in Devenport and Simpson[1]). The reason for this discrepancy between the original figure and the data in the ERCOFTAC database is not known.

Having established the good overall agreement between the calculated and measured mean flow characteristics in the junction region, we now turn our attention to the turbulence statistics. As already discussed, the presence of a pocket of intense turbulence production in the vicinity of the junction is one of the key findings of Devenport and Simpson.[1] This is shown in Fig. 7, which depicts measured and computed contours of turbulence kinetic energy (TKE) at the plane of symmetry. It should be kept in mind that the calculated TKE field contains only resolved contributions because the modeled contribution to the TKE cannot be readily computed from the SA model used in the DES. The experimental results reveal that the pocket of high TKE has a characteristic C shape with two distinct peaks. The first peak occurs near the wall while the second peak occurs at some distance above the wall approximately in the region occupied by the core of the mean HSV. As seen in this figure, the calculations capture this complex experimental trend with good accuracy. The computed TKE contours exhibit a very similar C structure with two peaks, one in the vicinity of the HSV core and the other just underneath it along the wall. The only notable discrepancy between measurements and calculations is the
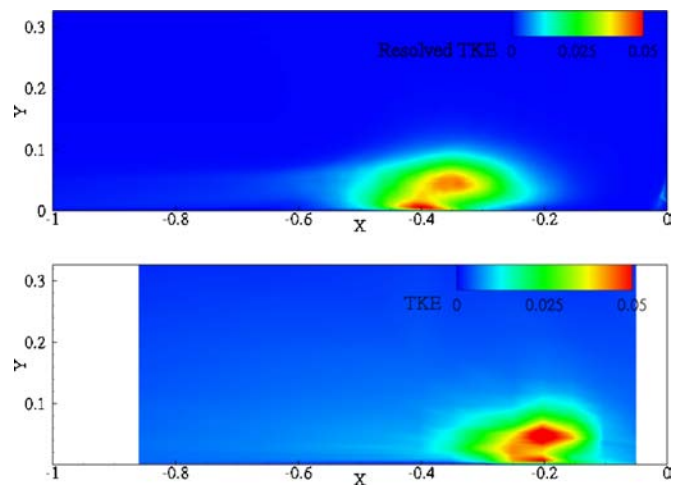
streamwise location of the pocket of high TKE, which in the calculations is further upstream from the wing than the measurements. This feature, however, is present throughout in our numerical solution as it is directly linked to the predicted mean location of the HSV. It is important to point out that previous RANS computations[10,11] have succeeded in capturing the peak of the TKE in the HSV core, but to the best of our knowledge the C-shaped structure of the contours and the existence of the second, near-wall peak have never been predicted numerically. As our subsequent discussion of the instantaneous resolved flow fields will show, the near-wall peak of the TKE field is linked to a complex instability mechanism that is responsible for the onset of the bimodal HSV dynamics. As such, it is not surprising that this important feature of the flow could not be captured with steady RANS models.

In Fig. 8, we show calculated and measured contours of the primary shear production term in the TKE equation. The calculated results include both the modeled and total stress production, see Figs. 8(a) and 8(b), respectively, in order to establish the fact that our simulation resolves directly essentially all significant scales of motion in the HSV region. The measured contours [see Fig. 8(c)] reveal the presence of an elongated pocket of intense positive TKE production in the vicinity of the HSV with a long, thin tail stretching upstream above and parallel to the wall. This tail marks the production of TKE by mean shear in the approaching turbulent boundary layer. It is clearly evident that the TKE production inside the boundary layer is one order of magnitude lower than that produced in the HSV core region. Another important feature of the laboratory flow is the existence of a pocket of intense negative production between the positive pocket and the wall. Negative TKE production signifies a reverse energy cascade from the small scales to large scales in the flow. This so-called backscattering effect is a characteristic of nonequilibrium turbulent flows, and in the context of the present case it suggests a complex interaction between near-wall generated small-scale structures and the coherent HSV—interestingly, a similar feature was reported in a recently published DNS of low Reynolds number flow past a wall-
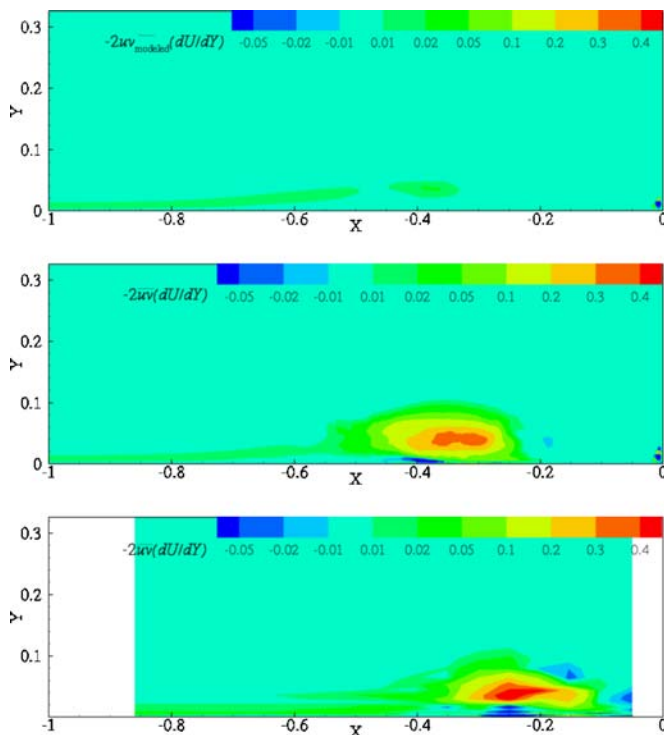
FIG. 8. Contours of the primary turbulence kinetic energy production at the plane of symmetry: (a) the modeled turbulence production, (b) the total (modeled+resolved) turbulence production, and (c) the measurement.[1]

mounted cube (see Yakhot *et al.*[18]). The calculated contours exhibit essentially all experimental features both qualitatively and quantitatively. The magnitude of positive and negative pockets of TKE production is well reproduced in our simulations. The computed results also capture the existence of a small pocket of weak negative TKE production downstream of the positive pocket, a trend that is also clearly visible in the measurements. It is important to note that unlike in LES, where the concept of backscattering refers to flow of energy from the unresolved to the resolved scales, in the present simulations the reverse energy cascade implied by the pockets of negative TKE production involves resolved scales of motion. That is, both the "small" and "large" scales involved in the exchange of energy in the HSV region are low-frequency, coherent motions of different scales. This is clearly evident from Fig. 8(a), which shows that the modeled TKE production is nonzero only inside the approaching boundary layer where the computational mesh is far too coarse to resolve turbulent motions. The exact nature of the interaction between the resolved small and large scales in the HSV region will be clarified in subsequent sections of this paper.

The results presented in this section have demonstrated the ability of the adjusted DES model to capture essentially all important experimental mean flow and turbulence statistics trends with good accuracy with the only exception being the precise location of the HSV, which in the simulations forms further upstream from the wing than in the measurements. In the subsequent sections, we turn our attention to the dynamics of the instantaneous flow in order to establish and explain the origin of the bimodal HSV oscillations.

B. The bimodal HSV dynamics at the symmetry plane

Devenport and Simpson[1] reported that the HSV undergoes bimodal, low-frequency oscillations between two basic states: the so-called *backflow* mode, when the return HSV flow—i.e., the flow that is directed from the wing leading edge toward the upstream direction along the flat plate—is able to penetrate far upstream forming a strong wall jet; and the *zero-flow* mode, when the return flow is unable to penetrate upstream and is ejected vertically upward away from the wall. The former mode is accompanied with large negative streamwise velocities in the region between the HSV and the wall and to the left (as viewed in the figure) side of the vortex, while the latter mode exhibits small positive values of streamwise velocity in the same region. Video animations of resolved velocity vectors at the symmetry plane show that our simulations reproduce this essential feature of the flow. Figure 9 shows two representative snapshots of calculated velocity vectors colored with out-of-plane vorticity contours at the symmetry plane, which depict clearly the backflow and zero-flow modes. Our results show that the flow field oscillates continuously and in a seemingly chaotic manner between these two basic states.

It is evident from Fig. 9(b) that the emergence of the zero-flow mode is accompanied by strong ejections of positive vorticity from the wall along the outer turn of the HSV, where the term "outer turn" refers to the left side of the HSV as viewed in the figure. To elucidate the rich vorticity dynamics of the flow in this region, we plot in Fig. 10 a series of representative snapshots of out-of-plane vorticity contours spanning a time interval that starts with the backflow state and ends with the zero-flow state. As seen in this figure, the transition from the backflow to the zero-flow mode is initiated by the interaction of the HSV with the wall, which leads to the extraction of a tongue of wall vorticity of opposite sign. The positive wall vorticity strengthens and lifts vertically upward engulfing the primary HSV. This strong initial interaction is seen to set off more complex secondary vortical interactions, which result in the emergence of multiple small pockets of positive vorticity [see Fig. 10(c)]. The ensuing complex, vortex-to-vortex interactions lead to the rapid breakdown of the primary HSV and cause the entire structure to retreat downstream toward the wing [Fig. 10(d)]. Following its destruction, the HSV reorganizes again, advances upstream away from the wing, and the entire process is repeated again in an aperiodic manner. The important conclusion that follows from this figure is that the interplay between the two states is governed by the interaction of the primary HSV with the wall. This complex interaction leads to the generation of wall vorticity of opposite sign, which ultimately leads to the obliteration of the HSV. Vortex-wall interactions leading to eruptive tongues of vorticity from the wall similar to those illustrated in Fig. 10 have also been documented in previous experimental studies of both laminar,[31] transitional,[33] and turbulent[6] HSV flows, but their underlying physical mechanisms are not entirely understood.[33] Doligalski *et al.*[33] has argued that the onset of eruptive tongues could be induced by the fact that a three-dimensional vortex in close proximity to the wall exposes the
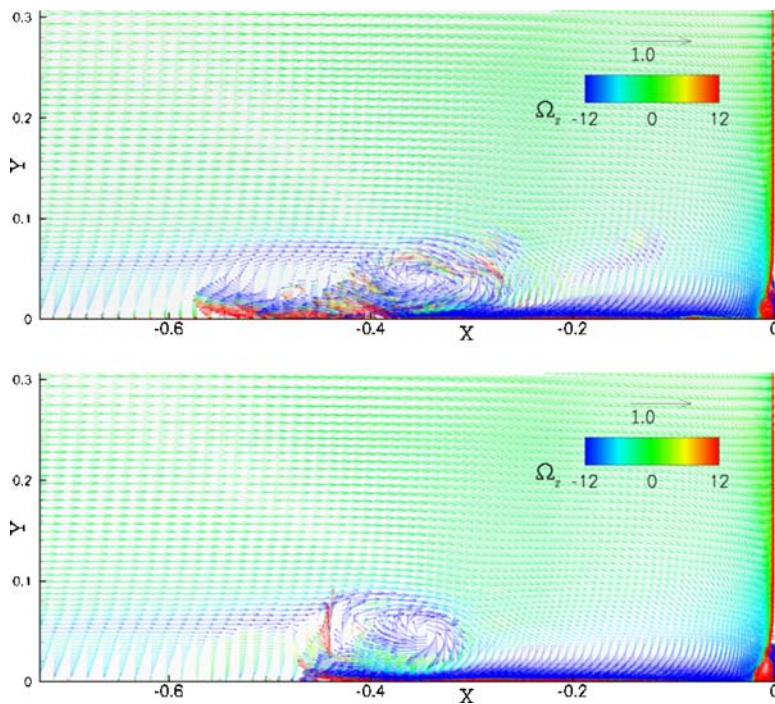
FIG. 9. Instantaneous velocity vectors colored by span-wise vorticity contours at (a) the backflow mode and (b) the zero-flow mode at the plane of symmetry.

wall to a strong local adverse pressure gradient that destabilizes the flow causing vortex-induced, three-dimensional separation. We shall discuss this topic further in a subsequent section of this paper, where we will elucidate the three-dimensional structure of the rich interactions of the HSV with the flat wall.

Figure 10 can also be used to explain the existence of the previously discussed near-wall peak in the TKE contours (see Fig. 7). It is evident from the snapshots shown in this figure, for instance, and video animation recordings that the flow between the HSV and the wall undergoes intense, low-frequency oscillations due to the continuous extraction of positive wall vorticity by the HSV and the ensuing rich vortical interactions. The intense low-frequency unsteadiness in this region is responsible for the near-wall peak in the TKE contours, while the continuous back and forth oscillation of the HSV along the wall due to the previously discussed vortex destruction and regeneration sequence causes the second TKE peak above the wall. Figure 10 also explains the presence of the region of negative TKE production below the HSV. As discussed before, negative production implies transfer of energy from small to large scales in the flow, and the process via which such transfer takes place is evident in Figs. 10(d) and 10(e). Small-scale structures of positive vorticity generated near the wall energize the HSV, leading to its subsequent destruction and retreat toward the wing.

To rigorously establish the bimodal dynamics of the HSV, we show in Fig. 11 a series of pdfs of the resolved streamwise velocity fluctuations at several locations along a vertically upward line at an axial location just upstream of the mean HSV core. The calculated pdfs are clearly bimodal, consisting of either two roughly Gaussian distributions or two peaks with different mean values. In the immediate vicinity of the wall, $y/T \leq 0.004$, the pdfs exhibit a dominant positive peak, which is associated with the zero-flow mode.

Recall that at the zero-flow mode, the near-wall streamwise velocities in the outer turn of the vortex tend to be positive as the return flow is unable to propagate upstream and erupts away from the wall. Juxtaposing this feature of the pdfs with the previously discussed vorticity dynamics (Fig. 10) reinforces further our previous conclusion that the zero-flow mode is due to the complex interaction of the HSV with the wall. As one moves upward away from the wall and in the region $0.004 < y/T < 0.02$, the second peak emerges in the calculated pdfs at negative streamwise velocity fluctuations. The calculated velocity histograms have two peaks of similar magnitude of pdfs in the upper edge of the thin positive vorticity layer underneath the mean HSV core in the region $0.0045 < y/T < 0.0065$ (see Fig. 4). In the outer part of the flow, the pdfs finally transition to a standard, single-peak, nearly Gaussian distribution around zero. It is important to note that the continuous transition of the calculated velocity histograms seen in this figure from a dominant positive peak near the wall, to the double peak structure in the vicinity of the top of the thin positive layer of vorticity, to the single peak Gaussian distribution in the vicinity of the mean HSV core, is identical to that observed in the measured pdfs of streamwise velocity fluctuations reported in Devenport and Simpson.[1]

C. POD analysis of resolved velocity fluctuations

To shed further insights into the nature of the bimodal dynamics of the HSV, we seek in this section to identify and study the dominant modes of the flow using proper orthogonal decomposition (POD). The POD approach was proposed as a technique for studying the dynamics of coherent structures in turbulent flows and for constructing low-dimensional dynamical representations of dynamically rich phenomena.[22]
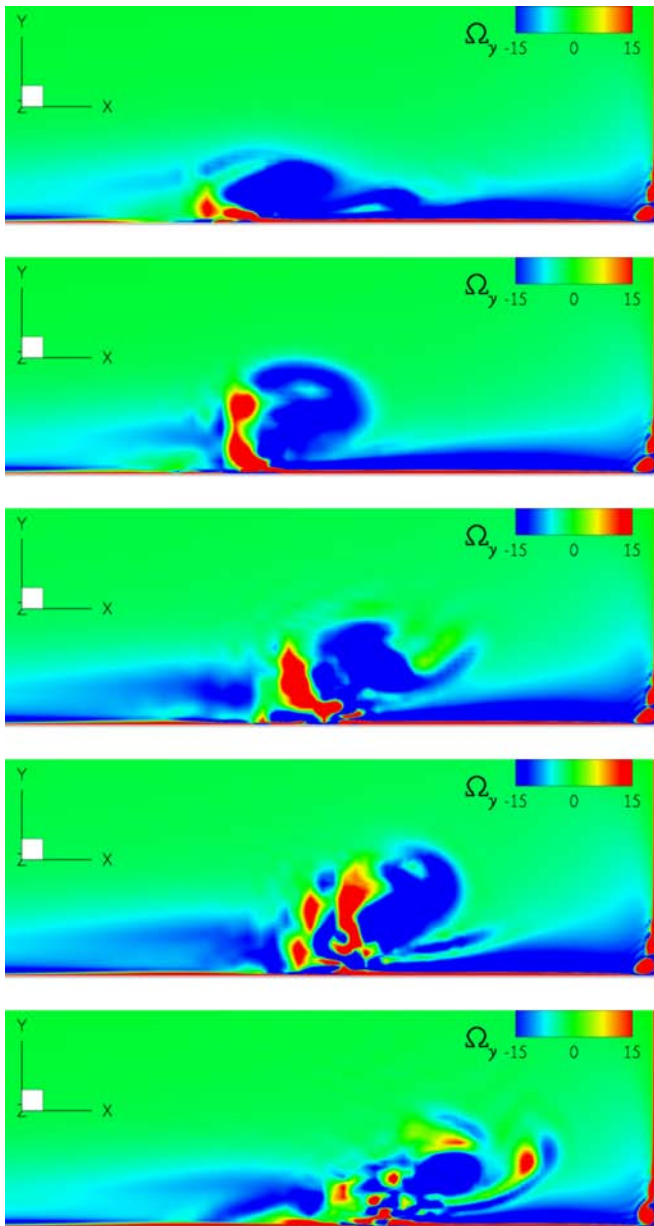
FIG. 10. Time sequence of computed instantaneous spanwise vorticity fields at the plane of symmetry upstream of the leading edge. Nondimensional time between snapshots is 0.49.
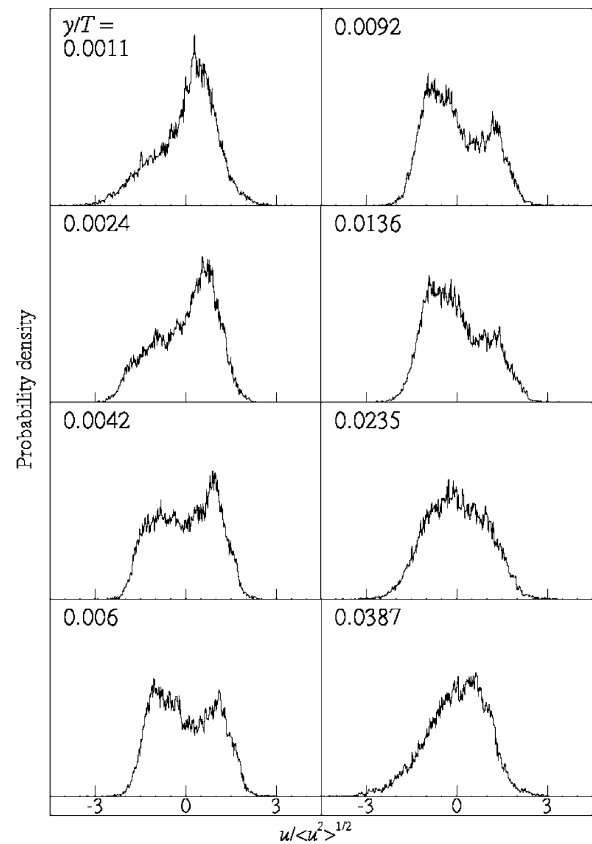

FIG. 11. Calculated probability density functions of streamwise velocity fluctuations along a vertical line across the core of a mean horseshoe vortex at the plane of symmetry.

As such, the POD is ideally suited for separating the underlying dominant modes in the flow and studying their properties.

The POD is the optimal linear representation of a set of data with empirical eigenfunctions. The original data of the streamwise resolved velocity fluctuations $[\upsilon(x,t)=u(x,t)-\langle u \rangle]$ is projected onto an orthonormal basis, and represented as a finite-dimensional sum[22]:

$$\upsilon(x,t) = \sum_{j}^{N} a_j(t)\varphi_j(x). \tag{10}$$

The optimal POD basis vectors φ_j are chosen to maximize the average projection of υ, which is equivalent to obtaining the vectors from the eigenvalues and eigenfunctions of the autocorrelation matrix of the computed results.[22] This en-

sures an orthogonal basis with uncorrelated modal coefficients, $a_j(t)$, and positive empirical eigenvalues λ_j that represent the energy contained in each mode.[22]

The first attempt to reconstruct the phase space of the HSV flow field using the standard POD methodology given in Holmes *et al.*[22] was not successful. We obtained a dominant first POD mode with double-peak pdf structure, i.e., the algorithm failed to separate the dominant modes. Extensive tests showed that this is due to the combined effects of unsteadiness and spatial variability of the HSV in the junction region, which do not permit for an effective modal separation of the velocity fluctuation time series. To remedy this situation, we adopted the procedure proposed by Horel,[34] which has been successfully applied to identify dominant modes in transient geophysical data sets. Following Horel,[34] we construct a complex representation of the velocity time series as follows:

$$z(x,t) = \upsilon(x,t) + i\hat{\upsilon}(x,t), \tag{11}$$

where $\hat{\upsilon}(x,t)$ is the Hilbert transform of the original time series $\upsilon(x,t)$ defined as the convolution between the original time series and the function $1/(\pi t)$:

$$\hat{\upsilon}(x,t) = \frac{1}{\pi}\int_{-\infty}^{\infty}\frac{\upsilon(x,\tau)}{t-\tau}d\tau. \tag{12}$$

The POD decomposition is then performed on the new complex time series given by Eq. (11) rather than the original

data. The discrete series transformation is calculated by interchanging the real and imaginary parts of the Fourier transform of the series, multiplying the data in frequency domain by $i=\sqrt{-1}$. This procedure corresponds to a filter operation applied to the velocity field, in which the amplitude of the Fourier components is maintained while its phase is advanced by a quarter of a cycle $\pi/2$.[34]

We apply the above procedure to analyze the streamwise velocity fluctuations at the symmetry plane on a vertical line across the time-average horseshoe vortex, at $X/T=-0.36$, up to a distance of $Y/T=0.0419$ above the wall. At each point along the prescribed transect, we employ time series spanning a total of 30000 time steps to obtain the eigenvalues and eigenfunctions of the correlation tensor. Figure 12(a) shows the relative magnitude of the twelve largest eigenvalues λ_j of the decomposition, which as discussed above represent the energy contained in each POD mode. It is clearly evident in this figure that the first two POD modes reproduce most of the variance of the velocity fluctuations, containing 85% of the streamwise turbulence kinetic energy.

The two dominant POD modes turn out to also contain the intrinsic bimodal physics of the unsteady horseshoe vortex as shown in Fig. 12(b), which shows the pdfs for the first two POD modes. The pdf of the first mode is very wide and exhibits a peak at negative velocity values. Thus, this POD mode corresponds well with the physical backflow mode of the HSV. The pdf of the second mode, on the other hand, is concentrated near zero and is thus consistent with the zero-flow mode of the HSV. Though not shown here, the pdfs from the third mode and beyond are zero-mean Gaussian distributions.

The structure of the eigenvalue spectrum obtained from the POD decomposition [see Fig. 12(a)] has important implications in the characterization of the coherent dynamics of the HSV system. As seen in Fig. 12(a), the decay of the eigenvalue magnitudes can be well described with the following exponential law: $\lambda_n \approx \exp(-cn)$, with $c=0.65$. This rapid exponential decay of energy with mode number suggests that all realizations of the system and consequently its underlying dynamics are controlled by a small number of modes.[22,35] To show that the first two POD modes essentially contain all important dynamics of the HSV, we compare in Fig. 12(c) the original streamwise velocity fluctuation time series at a point within the HSV with its POD reconstruction using only the first two POD modes. It is seen that the two-dimensional POD reconstruction can capture in detail the most significant time scales and features of the flow, including the highly intermittent positive excursions in a region of negative average streamwise velocity.

To explore the temporal characteristics of the streamwise velocity fluctuations, we plot in Fig. 13(a) the autocorrelation functions of the coefficients of the two dominant POD modes. Similar plots of all higher POD modes ($N>3$) reveal rapid loss of the temporal correlation as the corresponding autocorrelation functions decay to a white noise state within very short time. The two first POD modes, on the other hand, remain correlated for long times with each mode exhibiting a periodic-like variation. The respective power spectral densities of the first two modes are depicted in Fig. 13(b) and
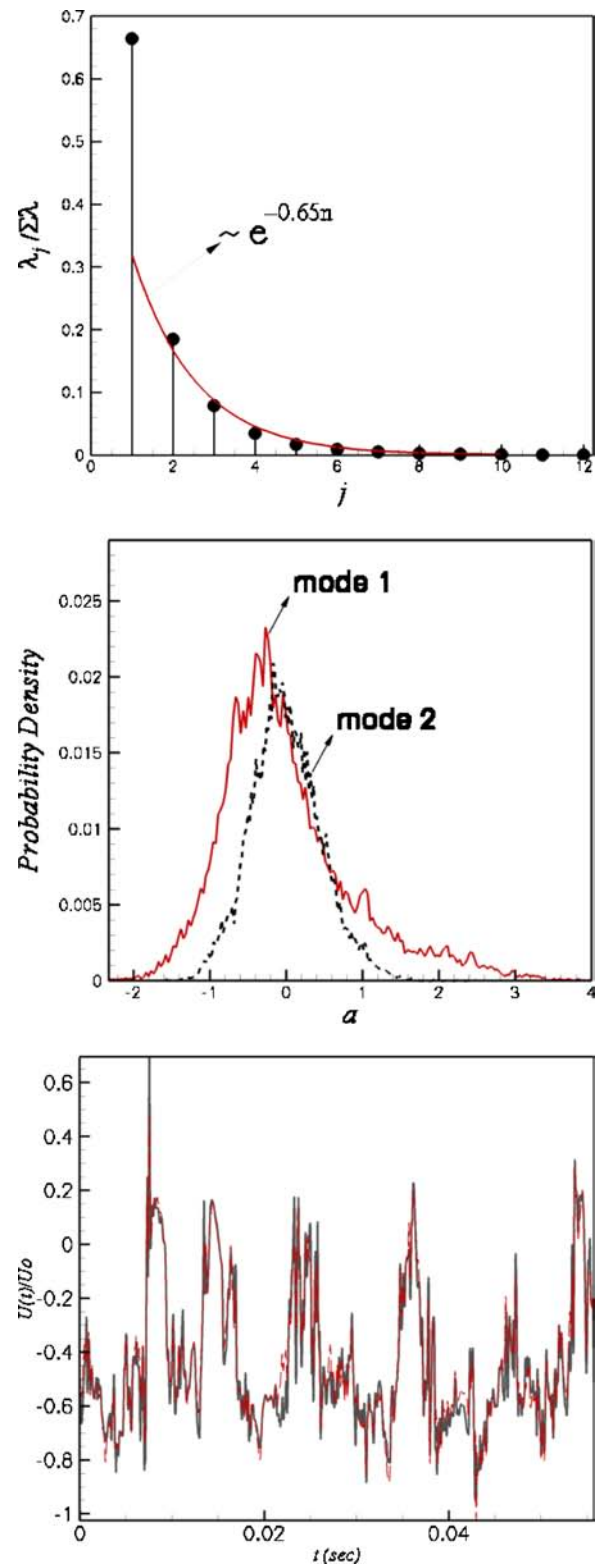

FIG. 12. POD analysis: (a) largest eigenvalues of the POD decomposition of the HSV system at $X/T=-0.36$ (first two modes contain 85% of the streamwise TKE); (b) histograms of the POD modal coefficients of the first two modes; (c) bimodal reconstruction of streamwise velocity (red dashed line) at $X/T=-0.36$, $Y/T=0.006$, compared to the original data series (black solid line).

clearly show the existence of a dominant frequency for each mode. The Mode 2 dominant frequency is $f=71.7$ Hz (Strouhal number St$=0.19$) with several harmonics that appear at higher frequencies. Mode 1 has a large energy accumulation
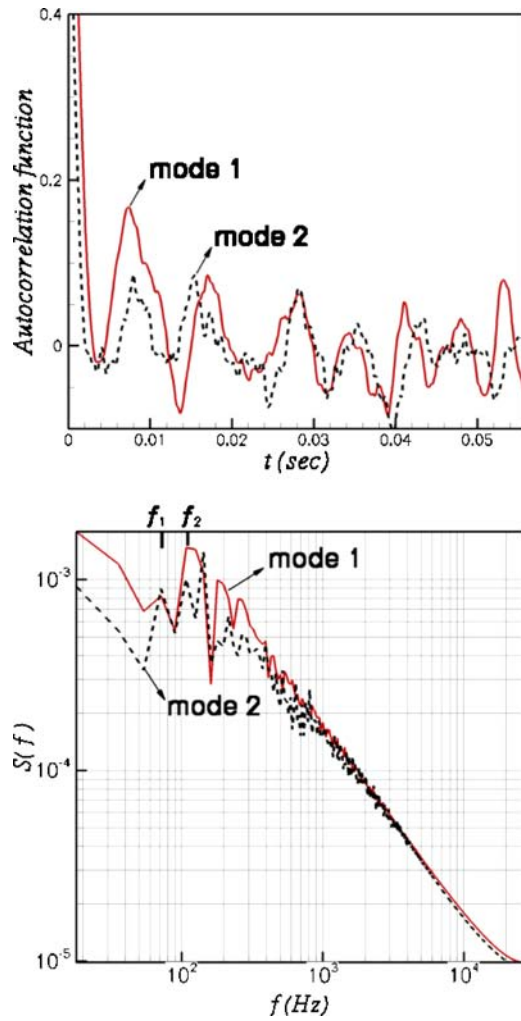
FIG. 13. POD analysis: (a) autocorrelation functions of the first two modes and (b) power spectral density of the same coefficients showing the quasi-periodicity of the HSV system.

at $f=107.6$ Hz (St=0.29). These frequencies are incommensurate, which, along with the fact that all essential dynamics is captured by the first two POD modes, points to the conclusion that the coherent HSV dynamics is quasiperiodic.

D. PDF-based conditional averaging

In previous sections, we have provided evidence based on instantaneous realizations of the flow that the onset of the bimodal dynamics of the HSV is associated with the complex interaction of the primary vortex with the wall and the extraction of tongues of positive vorticity. In order to firmly establish this important conclusion in a statistical sense, we propose herein a conditional averaging approach that is aimed at calculating averages of only realizations that correspond either to the backflow or to the zero-flow states. The procedure is summarized as follows.

Let (x_c, y_c) be a point at the symmetry plane, which is located somewhere in the vicinity of the mean HSV core. We shall denote this point as the control point and we will only require that the pdf of streamwise velocity fluctuations at this point is clearly bimodal—say like the one shown in Fig. 11 at $y/T=0.006$. Let v_c^- and v_c^+ denote the negative and positive

peaks of the bimodal pdf, respectively. We define the conditional average of the velocity field at every point (x_j, y_j) on the symmetry plane based on the pdf of the control point c as follows:

$$\langle u \rangle_j^{\pm} = \frac{1}{N^{\pm}} \sum_{n=1}^{N} \xi_n^{\pm} u_j(t^n), \qquad (13)$$

$$\xi_n^{\pm} = \begin{cases} 1 & \text{if } v_j(t^n) \in [v_c^{\pm} - \varepsilon, v_c^{\pm} + \varepsilon] \\ 0 & \text{otherwise} \end{cases}$$

where N is the number of total available realizations (i.e., the total number of time steps over which the simulation was carried out), ε is a small positive constant that defines the size of the averaging window around the positive or negative peak of the control point pdf, and $N^{\pm}$ denotes the number of realizations that fall within the positive or negative averaging window, respectively. Using the above notation, $N^{\pm}$ can be calculated as follows:

$$N^{\pm} = \sum_{n=1}^{N} \xi_n^{\pm}. \qquad (14)$$

In other words, according to Eq. (13), $\langle u \rangle_j^+$ is the average of only those realizations at point j for which the corresponding realization of the streamwise velocity fluctuation at the control point c falls within the defined window of width 2ε centered around the positive peak of the pdf of $v_c(t)$. The underlying hypothesis of this averaging procedure is that by using only one strategically selected control point at the symmetry plane, we can separate and average only realizations corresponding to either the backflow or zero-flow modes for the entire plane.

Figures 14(a) and 14(b) show the result of applying the so-describe conditional averaging procedure to the velocity field at the symmetry plane. The two figures show the resulting conditionally averaged velocity vectors and out-of-plane vorticity contours for the backflow and zero-flow states, respectively. The pdf of the control point along with the averaging windows are also included for reference. It is evident from these figures that the pdf-based conditional averaging can very effectively separate the two states. In fact, the effect of this averaging approach becomes even more profound if we subtract from the conditional averaged values the corresponding time-averaged values. That is, we define the following conditionally averaged fields:

$$\widetilde{\langle u \rangle}_j^{\pm} = \langle u \rangle_j^{\pm} - \langle u \rangle_j, \qquad (15)$$

where $\langle u \rangle$ denotes the standard Reynolds time average. The resulting velocity and vorticity fields for the two states are shown in Figs. 14(c) and 14(d), respectively. The contrast between the so-constructed states is striking as one appears to be nearly the mirror image of the other. For the backflow state, the velocity field exhibits only negative velocity components in the region of the HSV and the wall, while the reverse is true for the zero-flow state. Furthermore, the backflow state is characterized by a negative vorticity core occupying the region where the mean HSV is located along with a thin layer of positive wall vorticity that remains confined in
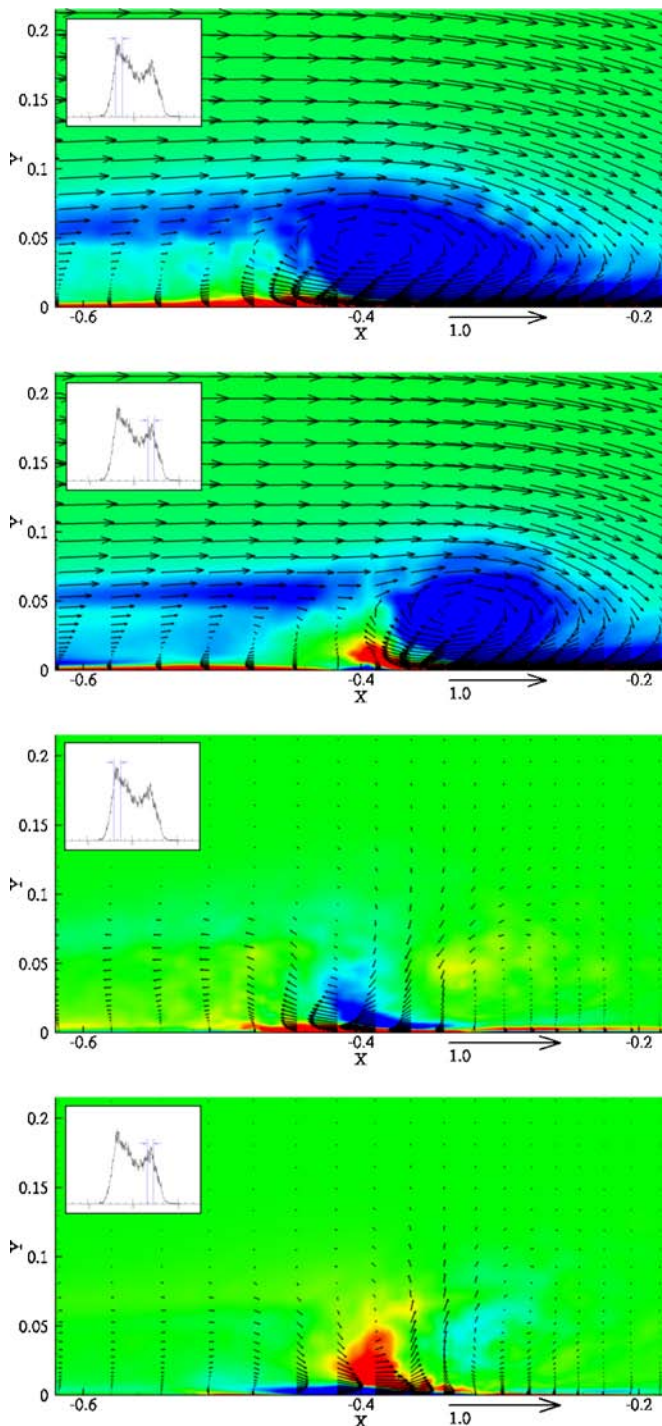
FIG. 14. The two modes of the bimodal oscillations visualized by the pdf-based conditional averaging: (a),(b) conditionally averaged velocity vectors calculated by Eq. (13) and (c),(d) their Reynolds-decomposed components calculated by Eq. (15) at (a),(c) the backflow mode and (b),(d) the zero-flow mode at the plane of symmetry. Contours show the corresponding spanwise vorticity distributions (blue, $\Omega_Z = -12$ and red, $\Omega_Z = +12$). Two blue lines in the inset of each figure stand for the width of the averaging window [i.e., 2ϵ in Eq. (13)].

the immediate vicinity of the wall. For the zero-flow state, on the other hand, the positive vorticity layer lifts off the wall and dominates the HSV region.

The conditional averaging approach developed in this section, therefore, establishes clearly the presence of the two
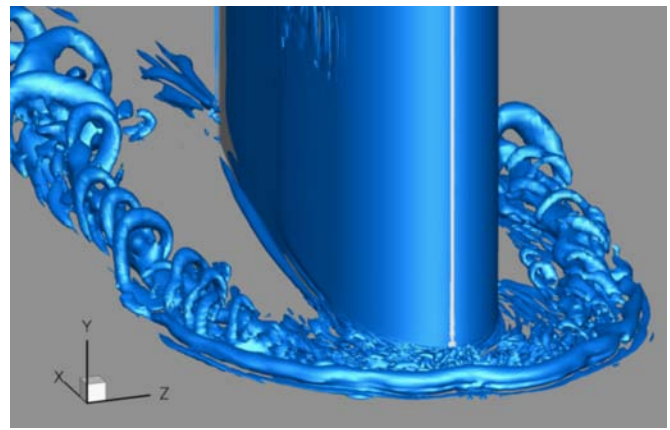

FIG. 15. Instantaneous snapshot of three-dimensional coherent structures around the wing visualized using the q criterion ($q = 1.0$).

basic states in a statistical sense. It further shows that the defining feature of the zero-flow mode is the formation of eruptive tongues of positive near-wall vorticity due to the interaction of the HSV and the flat plate. In the next section, we will elucidate and clarify the three-dimensional mechanism that causes this vorticity eruption phenomenon.

E. Three-dimensional visualization of the coherent structures

To identify the three-dimensional coherent dynamics of the HSV system, we employ the so-called q criterion, where q is defined as follows:[36]

$$q = \frac{1}{2}(\|\Omega\|^2 - \|\mathbf{S}\|^2), \tag{16}$$

where $\|\cdot\|$ is the Euclidean matrix norm and Ω and $\mathbf{S}$ denote the symmetric and antisymmetric parts of the velocity gradient, respectively. According to Hunt et al.,[36] regions where $q > 0$, i.e., regions where the rotation rate dominates the strain rate, are occupied by vortical structures. Although some deficiencies associated with local minima of the pressure and an imposed nonuniform strain field have been reported,[37] the q criterion identifies well coherent vortices with less sensitivity to numerical noise than the λ_2 method.[38,39] We apply the q criterion to the instantaneous resolved flow fields and construct video animations of the resulting coherent structures.

Figure 15 shows an instantaneous snapshot of a q criterion ($q = 1.0$) in the entire wing configuration in order to appreciate the overall complexity of the flow in the junction region. The flow around the wing is dominated by the very complex HSV system created by the roll up of the incoming flow due to the induced adverse pressure gradient. At the time instant shown in the figure, the resulting vortical structure consists of at least two necklace-like vortices wrapping around the wing. The primary vortex is thicker and forms at some distance above the flat wall. The secondary necklace-like structure is thinner and forms just above the wall in the outer part of the primary HSV. The formation of secondary vortical structure is presumably the result of the interaction between the primary HSV and the wall. The two necklace-

like structures wrap around the wing, where they begin to
intertwine. Their mutual interaction as well as their interac-
tion with the surrounding walls give rise to very complex
flow patterns with at least two rows of hairpin vortices form-
ing around the legs of the HSV system and in the region
between the HSV and the surface of the wing. Clearly the
coherent dynamics of the flow around the wing is very rich,
but a detailed examination of the flow in this region is be-
yond the scope of this paper. A more in-depth consideration
of the flow physics around and in the wake of the wing will
be left as a subject for future work. One limitation of the q
criterion is evident in Fig. 15 and should be noted here. The
viscous sublayer on the surface of the wing falsely appears as
a vortex according to the q definition. This is because shear
is very high inside the sublayer, and the q criterion by defi-
nition shows a vortex by visualizing the difference of two
very large numbers in this region.

The snapshot shown in Fig. 15 was selected to corre-
spond to an instant in time when a coherent HSV is clearly
visible around the wing. As we have already discussed, how-
ever, the flow structures in the wing leading edge region are
very dynamic due to the continuous interplay between the
backflow and zero-flow modes. Figure 16 shows representa-
tive snapshots of the q isosurface within a time interval that
spans one complete transition from the backflow state, to the
zero-flow state, and back to the reestablishment of the back-
flow state. The initial instant shown in Fig. 16(a) corresponds
to the backflow state. A coherent HSV core is observed up-
stream of the wing leading edge, while in the region adjacent
to the wing the flow is very complex with multiple small-
scale structures. An important feature of the HSV at this
stage, which is visible in this figure, is the growth and propa-
gation of disturbances along the coherent HSV core. The
disturbances are marked by the distinct knot-like pattern that
develops along the vortex core at several locations, and their
emergence triggers the subsequent instability. The instability
originates in the region between the outer turn of the HSV
and the bottom wall, and is marked by the emergence of
multiple hairpin-like vortices, as seen in Fig. 16(b). The hair-
pins originate underneath the HSV and their legs are oriented
perpendicular to the HSV core and stretched along the wall
in the streamwise direction. The heads of the hairpins lift off
the wall and coil around the HSV core. The number of hair-
pins is not always constant but varies in an aperiodic manner.
From our video animations, we have been able to observe
realizations of the instability with anywhere from three to six
hairpin vortices. As the hairpin vortices engulf the HSV, they
disorganize it rapidly, essentially grinding it up, and cause it
to retreat downstream closer to the wing, as shown in Fig.
16(c). Juxtaposing the images in this figure with previously
discussed two-dimensional images, say Figs. 9 and 10, can
now help us to clarify important features of the zero-flow
mode such as the large vertical velocities in the outer turn of
the HSV (see Fig. 9) and the eruption of tongues of positive
vorticity from the wall (Fig. 10). Both of these phenomena
are 2D manifestations of the growth of the hairpin vortices
and their subsequent eruption from the wall to engulf and
destroy the HSV. As the destruction of the HSV is completed
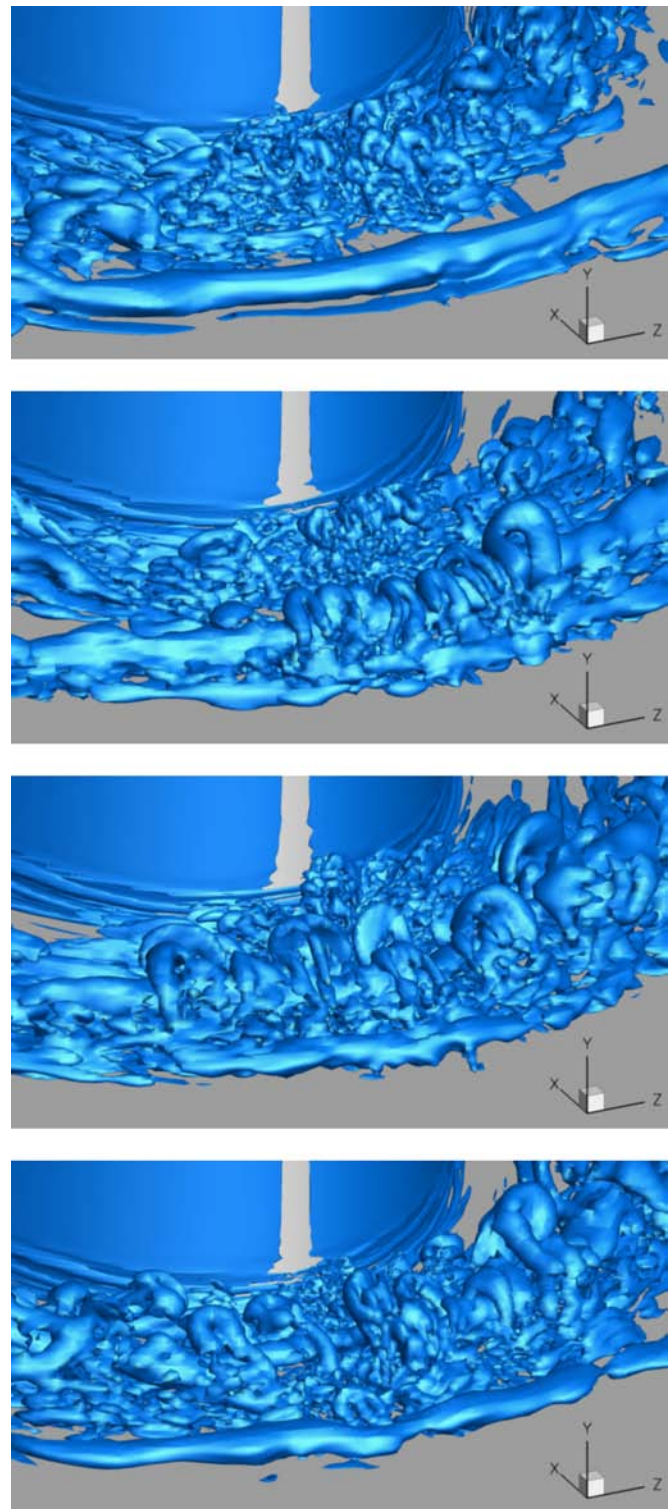by the hairpin vortices, a new coherent vortex core begins to

FIG. 16. Instantaneous sequential snapshots of three-dimensional coherent
structures visualized using the q criterion ($q=6.0$) in the vicinity of the
leading edge depicting one complete transition from (a) the backflow state;
(b), (c) the zero-flow state; and (d) back to the reemergence of the backflow
state (enhanced online).

emerge upstream of the wing. The rebirth process of the
HSV (or the reemergence of the backflow mode) is seen in
Figs. 16(c) and 16(d). Note that the formation of a new co-
herent vortex is essential as the approaching boundary layer
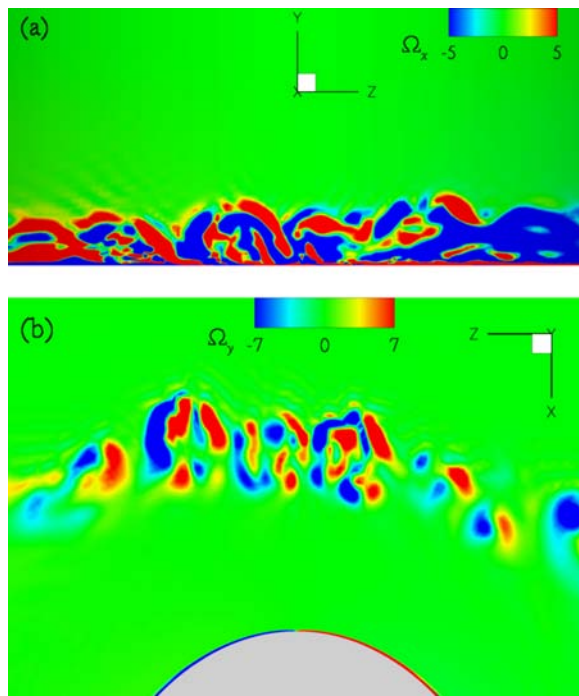continues to experience and cannot sustain the imposed ad-

FIG. 17. Calculated instantaneous vorticity contours at the instant of the emergence of the zero-flow mode corresponding to Fig. 16(b): (a) front view of the streamwise vorticity distribution in a vertical (y-z) plane across just upstream of the primary HSV and (b) top view of the vertical vorticity distribution in a horizontal (x-z) plane across the upper part of the primary HSV.

verse pressure gradient and should roll up again and separate to form the HSV. Following the formation of the new coherent HSV core, however, disturbances begin to grow along its core and the destruction scenario described above is repeated again.

The question that naturally emerges from the above discussion is with regard to the instability mechanism that gives rise to the hairpin vortices ultimately destroying the HSV. The key to answering this question can be found in the orientation of the legs of the hairpin vortices relative to the flow and the HSV core. Unlike the hairpin vortices that grow downstream of the leading edge whose legs are aligned with the HSV core (see Fig. 15), the legs of the hairpins in the junction region are perpendicular to the HSV core and are oriented in the streamwise direction. This orientation implies the generation of streamwise vorticity in the vicinity of the plane of symmetry. To illustrate this feature of the flow, we show in Fig. 17(a) instantaneous streamwise vorticity contours at a x=const (vertical) plane that passes through the HSV near its outer turn. This figure clearly shows the formation of pairs of counter-rotating streamwise vortices. As these streamwise structures emerge from underneath the HSV, they curve upward and adjacent counter-rotating pairs join together to form hairpins. The resulting vorticity field on a horizontal cross section through the heads on these hairpins is shown in Fig. 17(b).

We argue that the HSV instability that leads to the emergence of the hairpin vortices is centrifugal in nature and is the result of the interaction of the HSV with the wall. The instability originates along the outer turn of the vortex where
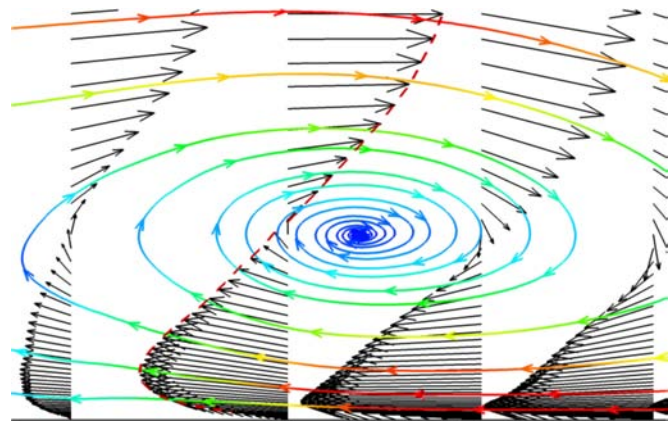

FIG. 18. Calculated, pdf-based conditionally averaged streamlines and velocity vectors at the backflow mode depicting the near-wall inflection point of the velocity profile and the convex curvature of the streamlines in the same region. The streamlines are colored by the magnitude of the velocity.

the curvature of the streamlines is concave, as shown in Fig. 18. Due to the presence of the wall underneath the vortex, the velocity profile in this region exhibits an inflection point (see Fig. 18), which results in the formation of a near-wall layer within which the velocity magnitude is decreasing with the radius of curvature. According to the stability criterion proposed by Floryan,[40] a boundary layer developing along a curved wall exhibits the potential for centrifugal instability if the velocity magnitude decreases with the radius of curvature. It is evident from Fig. 18 that Floryan's criterion is readily satisfied in the near-wall layer underneath the HSV. Furthermore, the flow in this region also satisfies Lord Rayleigh's inviscid criterion[41] for centrifugal instability. In Fig. 19, we plot the variation of Rayleigh's quotient $\Phi(r) = \partial(ru_\theta)/\partial r$ along the vertical line that starts from the mean HSV core location and ends at the wall. The radius r is measured from the vortex core and the angular velocity coincides for this radius with the streamwise velocity. As seen in Fig. 19, Lord Rayleigh's condition for centrifugal instability $\Phi(r) < 0$ is indeed satisfied between the HSV and the wall.
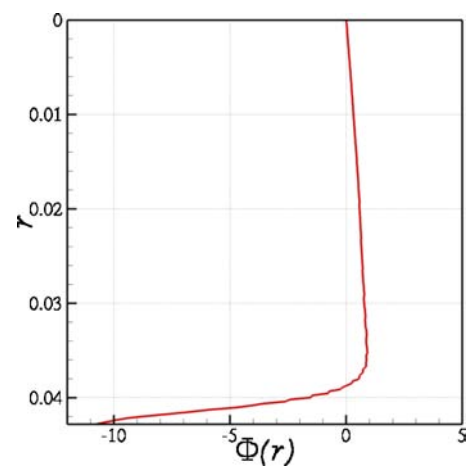

FIG. 19. Variation of Rayleigh's quotient $\Phi(r) = \partial(ru_\theta)/\partial r$ along the vertical line that starts from the mean HSV core location ($r=0$) and ends at the wall.

In the case of a turbulent boundary layer developing over a continuous concave wall, the instability develops in the form of counter-rotating longitudinal Görtler vortices. In the present flow, however, the instability originates in the form of counter-rotating vortices, but because the exposure to curvature is only local, in the immediate vicinity of the outer turn of the HSV, adjacent streamwise vortex pairs emerging from underneath the HSV appear to join together to form hairpin vortices. Interestingly, the connection between the near-wall inflection point of the velocity profile and the instability of the HSV was first made by Agui and Andreopoulos.[6] In their flow visualization experiments, they described the eruptions of mushroom-like vortical structures originating between the wall and the HSV forming in the upstream junction region of a wall-mounted cylinder. They commented that the eruptions of mushroom-like vortices from the wall occur at instances when a strong backflow is formed between the wall and the HSV, i.e., when the local velocity profiles assume a wall-jet-like shape.[6]

The instability we uncover herein as well as that described by Agui and Andreopoulos[6] appear to be very similar to the instability reported in the recent experimental work of Allen and Naitoh,[42] who studied the flow generated in the region where a moving flat wall slides under a stationary one. Above a threshold Reynolds number, the moving near-wall flow at the junction of the two walls rolls up to form a coherent 2D vortex that subsequently interacts with the stationary wall in a manner closely resembling the interaction of the HSV with the flat wall in the vicinity of the plane of symmetry. Allen and Naitoh[42] showed that as the moving wall speed increases, spanwise disturbances develop along the vortex core, eventually leading to the emergence of mushroom-like vortical structures that grow in the region between the outer turn of the vortex and the stationary wall. The flow visualization pictures of Allen and Naitoh[42] clearly show these mushroom-like vortices to lift off the wall and engulf the primary vortex in a manner similar to that shown in Fig. 16. Allen and Naitoh[42] pointed out the similarity between their flow and the 3D driven cavity flow, where mushroom-like vortical structures have been shown to develop in the region between the primary and downstream secondary eddies near the downstream lower corner of the cavity (see Koseff and Street[43] and Aidun, Triantafillopoulos, and Benson[44] for details). The emergence of these structures is now widely accepted to be due to centrifugal instability of the curved shear layer between the primary and secondary eddies of the cavity.[43] In this region of the cavity flow, the velocity variation with the local radius of streamline curvature is very similar to that in the Allen and Naitoh[42] flow and the present flow in the region between the outer turn of the vortex and the wall. Allen and Naitoh[42] analyzed their experimental data to show that the Rayleigh criterion for centrifugal instability is indeed satisfied in this region (as in our case) and provided evidence suggesting that the spanwise wavelengths selected in their experiment are within the range of those predicted by theoretical stability considerations.[40]

In summary, our results when considered collectively with the early cavity work of Koseff and Street[43] and the recent work of Allen and Naitoh[42] point to the conclusion

that centrifugal instability could be an important mechanism inherent to flows involving the interaction of a vortex with a solid wall. In lieu of these findings, one can now reasonably argue that the complex eruptive phenomena observed in various situations where a vortex interacts with a wall[6,33,45] could be the result of centrifugal instability due to the combination of the local streamline curvature imposed by the vortex and the inflection point in the velocity profile caused by the proximity of the vortex to the wall.

IV. CONCLUSIONS

We have carried out numerical simulations of turbulent flow past the wing-body junction configuration studied experimentally by Devenport and Simpson[1] using the DES approach with an adjusted length scale. Comparisons between the calculated solutions and time-averaged vorticity measurements and turbulence statistics at the plane of symmetry in the junction region showed that the model captures most experimental trends with good qualitative and quantitative accuracy. The instantaneous resolved flow fields also exhibit all trends observed in the experiment. The HSV is found to oscillate aperiodically between the two basic flow states documented in the experiment of Devenport and Simpson.[1] Furthermore, the calculated streamwise fluctuations exhibit the experimentally documented bimodal pdfs in the vicinity of the HSV with two clearly defined peaks around a negative and a (close to zero) positive value, respectively.

The only remaining discrepancy between the simulations and the measurements is the predicted location of the mean HSV core, which occurs somewhat upstream of the measured location. The reasons for this discrepancy are not entirely clear. Previous steady RANS studies[8–11] have clearly shown that the prediction of the HSV location is very susceptible to the specific RANS turbulence model. So one possible reason for this discrepancy could be the base Spalart-Allmaras model used in the DES, and future work should focus on exploring this issue by considering DES formulations with other base turbulence models. Another clue for a possible explanation is suggested by LES studies of flow past a wall mounted cube.[12–15] As shown in Krajnović and Davidson,[15] for instance, LES with steady inflow conditions tend to predict a HSV that is located upstream of the measured location. LES with turbulent-like inflow conditions, on the other hand, appear to yield the correct vortex location.[14] The issue of time-varying inflow boundary conditions, however, is not so straightforward to address in the context of DES as the upstream grid is far too coarse to support LES, turbulent-like inflow conditions.

The resulting good overall agreement with the measurements allowed us to probe into the physics of the turbulent HSV using a variety of coherent structure analysis and visualization techniques (POD, conditional averaging, etc.) and propose the following mechanism for the onset of the bimodal coherent dynamics. The backflow state identified in the experiment of Devenport and Simpson[1] corresponds to a well organized, coherent HSV that forms as the approaching boundary layer separates due to the induced adverse pressure gradient. The formation of the HSV above the flat wall, how-

ever, contains the seeds of its own subsequent obliteration. The velocity profile in the region between the outer turn of the HSV and the wall develops an inflection point due to the presence of the wall, which, combined with the local streamline curvature due to the HSV sense of rotation, sets up a potentially unstable situation near the outer turn of the vortex. Görtler-like pairs of counter-rotating streamwise vortices originate underneath the HSV. As adjacent pairs lift off the wall, they join together to form hairpins. The hairpins grow and wrap around the HSV, causing it to break down and to retreat backward toward the wing surface. The resulting disorganized state corresponds to the one dubbed by Devenport and Simpson as the zero-flow mode as it is accompanied by large vertical velocities along the outer turn of the vortex and eruptions of tongues of wall vorticity associated with the formation of the hairpin vortices. Following its destruction, a coherent HSV forms again in the junction region because the approaching boundary layer continues to be exposed to the same adverse pressure gradient induced by the presence of the wing and should separate. The entire process repeats itself all over again in a quasiperiodic manner.

Our work has demonstrated the potential of DES as a powerful simulation tool for predicting complex, high Reynolds number flows dominated by organized coherent structures using modest computational resources. The success of our simulations, however, depended critically on the flow-specific adjustment of the DES length scale we had to implement in order to suppress the well-known shortcoming of DES, that or grid-induced premature separation. This adjustment worked well for the present flow, but obviously it does not constitute a general model. The success of our simulations did demonstrate, however, that research efforts aimed at developing a generally applicable DES formulation that is not sensitive to the computational grid can be especially rewarding. One such effort was recently reported by Spalart *et al.*[46] They proposed a new DES limiter that seeks to accomplish essentially the same objective we accomplished for the specific junction flow in this work—namely to delay the onset of the LES mode of the model—but in a general manner. The new DES model is dubbed the delayed DES (DDES) approach and utilizes a modified DES length scale, which depends on the local resolved velocity gradients in the flow. We are currently in the process of evaluating the DDES approach for the HSV flow, and we will be reporting our findings in a future communication.

ACKNOWLEDGMENTS

[1]W. J. Devenport and R. L. Simpson, "Time-dependent and time-averaged turbulence structure near the nose of a wing-body junction," J. Fluid Mech. **210**, 23 (1990).
[2]R. Martinuzzi and C. Tropea, "The flow around surface-mounted, prismatic obstacles placed in a fully developed channel flow," J. Fluids Eng. **115**, 85 (1993).
[3]H. Hussein and R. J. Martinuzzi, "Energy balance for turbulent flow around a surface mounted cube placed in a channel," Phys. Fluids **8**, 764 (1996).
[4]C. J. Baker, "The turbulent horseshoe vortex," J. Wind. Eng. Ind. Aerodyn. **6**, 9 (1980).
[5]B. Dargahi, "The turbulent flow field around a circular cylinder," Exp. Fluids **8**, 1 (1989).
[6]J. H. Agui and J. Andreopoulos, "Experimental investigation of a three dimensional boundary layer flow in the vicinity of an upright wall mounted cylinder," J. Fluids Eng. **114**, 566 (1992).
[7]R. L. Simpson, "Junction flows," Annu. Rev. Fluid Mech. **33**, 415 (2001).
[8]H. C. Chen, "Assessment of a Reynolds stress closure model for appendage-hull junction flows," J. Fluids Eng. **117**, 557 (1995).
[9]S. Fu, T. Rung, F. Thiele, and Z. Zhai, in *Proceedings of the 11th Symposium on Turbulent Shear Flows*, edited by M. Lesieur, B. E. Launder, G. Binder, and J. H. Whitelaw (Grenoble, France, 1997), pp. 6.7–6.12.
[10]S. Parneix, P. A. Durbin, and M. Behnia, "Computation of 3-D turbulent boundary layers using the V2F model," Flow, Turbul. Combust. **60**, 19 (1998).
[11]D. Apsley and M. Leschziner, "Investigation of advanced turbulence models for the flow in a generic wing-body junction," Flow, Turbul. Combust. **67**, 25 (2001).
[12]W. Rodi, "Comparison of LES and RANS calculations of the flow around bluff bodies," J. Wind. Eng. Ind. Aerodyn. **69**, 55 (1997).
[13]W. Rodi, J. Ferziger, M. Breuer, and M. Pourquié, "Status of large-eddy simulation: Results of a workshop," J. Fluids Eng. **119**, 248 (1997).
[14]K. B. Shah and J. H. Ferziger, "A fluid mechanicians view of wind engineering: Large eddy simulation of flow past a cubic obstacle," J. Wind. Eng. Ind. Aerodyn. **67**, 211 (1997).
[15]S. Krajnović and L. Davidson, "Large-eddy simulation of the flow around a bluff body," AIAA J. **40**, 927 (2002).
[16]D. Lakehal and W. Rodi, "Calculation of the flow past a surface-mounted cube with two-layer turbulence models," J. Wind. Eng. Ind. Aerodyn. **67**, 65 (1997).
[17]G. Iaccarino, A. Ooi, P. A. Durbin, and M. Behnia, "Reynolds averaged simulation of unsteady separated flow," Int. J. Heat Fluid Flow **24**, 147 (2003).
[18]A. Yakhot, H. Liu, and N. Nikitin, "Turbulent flow around a wall-mounted cube: A direct numerical simulation," Int. J. Heat Fluid Flow **27**, 994 (2006).
[19]P. R. Spalart, W. H. Jou, M. Strelets, and S. R. Allmaras, in *Advances in DNS/LES*, edited by C. Liu and Z. Liu (Greyden, Columbus, OH, 1997).
[20]E. G. Paterson and L. J. Peltier, "Detached-eddy simulation of high-Reynolds-number beveled-trailing-edge boundary layers and wakes," J. Fluids Eng. **127**, 897 (2005).
[21]F. R. Menter, M. Kuntz, and R. Bender, "A scale-adaptive simulation model for turbulent flow predictions," AIAA Paper 2003-0767 (2003).
[22]P. Holmes, J. L. Lumley, and G. Berkooz, *Turbulence, Coherent Structures, Dynamical Systems and Symmetry* (Cambridge University Press, Cambridge, 1996).
[23]P. R. Spalart and S. R. Allmaras, "A one-equation turbulence model for aerodynamic flows," Rech. Aerosp. **1**, 5 (1994).
[24]K. D. Squires, J. R. Forsythe, and P. R. Spalart, "Detached-eddy simulation of the separated flow over a rounded-corner square," J. Fluids Eng. **127**, 959 (2005).
[25]M. Shur, P. R. Spalart, M. Strelets, and A. Travin, in *Turbulent Shear Flows*, edited by W. Rodi and D. Laurence (Elsevier Science, Amsterdam, 1999), pp. 669–678.
[26]F. Sotiropoulos and S. Abdallah, "The discrete continuity equation in primitive variable solutions of incompressible flow," J. Comput. Phys. **95**, 212 (1991).
[27]J. Paik, F. Sotiropoulos, and M. J. Sale, "Numerical simulation of swirling flow in a hydroturbine draft tube using unsteady statistical turbulence models," J. Hydraul. Eng. **131**, 441 (2005).
[28]J. Paik, L. Ge, and F. Sotiropoulos, "Toward the simulation of complex 3D shear flows using unsteady statistical turbulence models," Int. J. Heat Fluid Flow **25**, 513 (2004).
[29]J. Paik and F. Sotiropoulos, "Coherent structure dynamics upstream of a

long rectangular block at the side of a large aspect ratio channel," Phys. Fluids **17**, 115104 (2005).

[30] L. H. Norris and W. C. Reynolds, Report FM-10, Dept. of Mech. Eng., Stanford University, Stanford, CA (1975).

[31] C. V. Seal, C. R. Smith, O. Akin, and D. Rockwell, "Quantitative characteristics of a laminar necklace vortex system at a rectangular block-flat plate juncture," J. Fluid Mech. **286**, 117 (1995).

[32] H. D. Pasinato, K. D. Squires, and R. P. Roy, "Assessment of Reynolds-averaged turbulence models for prediction of the flow and heat transfer in an inlet vane-endwall passage," J. Fluids Eng. **126**, 305 (2004).

[33] T. L. Doligalski, C. R. Smith, and J. D. A. Walker, "Vortex interactions with walls," Annu. Rev. Fluid Mech. **26**, 573 (1994).

[34] J. D. Horel, "Complex principal components analysis," J. Clim. Appl. Meteorol. **23**, 1660 (1984).

[35] L. Sirovich, "Chaotic dynamics of coherent structures," Physica D **37**, 126 (1989).

[36] J. C. R. Hunt, A. A. Wray, and P. Moin, in *Proceedings of the Summer Program* (Center for Turbulence Research, NASA Ames/Stanford University, 1988), pp. 193–208.

[37] J. Jeong and F. Hussain, "On the identification of a vortex," J. Fluid Mech. **285**, 69 (1995).

[38] Y. Dubief and F. Delcayre, "On coherent-vortex identification in turbulence," J. Turbul. **1**, 1 (2000).

[39] K. Fraňa, J. Stiller, and R. Grundmann, "Taylor-Görtler vortices in the flow driven by a rotating magnetic field in a cylindrical container," J. Visualization **8**, 323 (2005).

[40] J. M. Floryan, "Görtler instability of boundary layers over concave and convex walls," Phys. Fluids **29**, 2380 (1986).

[41] Lord Rayleigh, "On the dynamics of revolving fluids," Scientific Paper **6**, 447 (1916).

[42] J. J. Allen and T. Naitoh, "Scaling and instability of a junction vortex," J. Fluid Mech. **574**, 1 (2007).

[43] J. R. Koseff and R. L. Street, "The lid-driven cavity flow: A synthesis of qualitative and quantitative observations," J. Fluids Eng. **106**, 390 (1984).

[44] C. K. Aidun, N. G. Triantafillopoulos, and J. D. Benson, "Global stability of a lid-driven cavity with throughflow: Flow visualization studies," Phys. Fluids A **3**, 2081 (1991).

[45] A. Yakhot, T. Anor, H. Liu, and N. Nikitin, "Direct numerical simulation of turbulent flow around a wall-mounted cube: Spatio-temporal evolution of large-scale vortices," J. Fluid Mech. **566**, 1 (2006).

[46] P. Spalart, S. Deck, M. Shur, K. Squires, M. Strelets, and A. Travin, "A new version of detached-eddy simulation, resistant to ambiguous grid densities," Theor. Comput. Fluid Dyn. **20**, 181 (2006).